THE MICROSTRUCTURAL EVOLUTION OF ZIRCONIA CERAMICS DURING SINTERING

by

Tiandan Chen

B.S., Tongji University, China 2000

Submitted to the Graduate Faculty of

the School of Engineering in partial fulfillment

of the requirements for the degree of

Master of Science

University of Pittsburgh

2006

UNIVERSITY OF PITTSBURGH

SCHOOL OF ENGINEERING

This thesis was presented

by

Tiandan Chen

It was defended on

August 31, 2006

and approved by

Pradeep P. Fulay, Professor, Materials Science and Engineering

John P. Leonard, Assistant Professor, Materials Science and Engineering

Thesis Advisor: Ian Nettleship, Associate Professor, Materials Science and Engineering

THE MICROSTRUCTURAL EVOLUTION OF ZIRCONIA CERAMICS DURING SINTERING

Tiandan Chen, M.S.

University of Pittsburgh, 2006

ZrO_2-3mol%Y_2O_3 powders were pressed uniaxially using loads of 51 MPa and isothermal sintered at 1275^{O}C. Measurements of the pore size, grain size and pore distribution indicated that contrary to the assumption of the phenomenological models of sintering, pore elimination was involved in densification and coarsening during the intermediate stage sintering. SEM imaging showed that many triple points did not contain pores. Thus the pore separation rather than the grain size should correlate with diffusion length. Pore boundary tessellation showed that the elimination of fine pores resulted in a heterogeneous microstructure in intermediate stage sintering containing regions of high solid volume fraction (>0.9).

Higher pressing pressure (238 MPa) or higher sintering temperature (1315 ^{O}C) resulted in a higher densification rate and microstructural heterogeneity over a larger length scale.

TABLE OF CONTENTS

TABLE OF CONTENTS V

LIST OF TABLES VII

LIST OF FIGURES VIII

ACKNOWLEDGEMENTS XIII

1.0 INTRODUCTION 1

2.0 BACKGROUND 3

2.1 SINTERING 3

2.1.1 Driving force of sintering 3

2.1.2 Flux of atoms 3

2.1.3 Sintering stages 7

2.1.4 Traditional model of single-phase sintering and predictive capability 10

2.2 THE MASTER SINTERING CURVE 13

2.2.1 Combined-stage sintering model 13

2.2.2 The master sintering curve (MSC) 15

2.3 EFFECT OF POWDER PROCESSING VARIABLES 18

2.3.1 Effects of powder processing on green density 19

2.3.2 Effects on densification and microstructure evolution 21

3.0 EXPERIMENTAL PROCURE 23

3.1 SAMPLE PREPARATION 23

3.1.1 Preparation of green bodies 23

3.1.2 Sintering 24

3.1.3 Sample section and preparation for polishing 25

3.1.4 Grinding and polishing 25

3.1.5 Thermal etching 26

3.2 MICROSCOPY 26
3.3 DATA ANALYSIS 27
3.3.1 Measurement of densities 27
3.3.2 Calculation of isothermal densification rate 28
3.3.3 Measurement of average pore size, pore separation, and grain size 29
3.3.4 Measurement of solid area fraction and number of pores per unit area 30
3.3.5 Measurement of mesoscale properties 31
4.0 RESULTS AND DISCUSSION 35
4.1 DENSIFICATION 35
4.2 AVERAGE GRAIN INTERCEPT, PORE SIZE AND PORE SEPARATION 41
4.3 PORE SIZE AND DISTRIBUTION FOR LPLT SAMPLES 47
4.4 TESSELLATOR RESULT OF LPLT SAMPLES 49
4.5 MICROSTRUCTURAL ANALYSES OF HPLT AND LPHT SAMPLES . 57
5.0 CONCLUSIONS 66
6.0 FUTURE WORKS 67
BIBLIOGRAPHY 68

LIST OF TABLES

Table 1. Values of L_L and Vv 58

LIST OF FIGURES

Figure 1 : **Illustration of the two-sphere sintering model geometry. The neck radius is given by r and the particle radius is a.** 4

Figure 2 : (a) Initial stage of sintering; model structure represented by spheres in tangential contact. (b) Near end of initial stage. Spheres have begun to coalesce. The neck growth illustrated is for center-center shrinkage of 4%. (c) Intermediate stage; dark grain have adopted shape of tetrakaidecahedron, enclosing white pore channels at grain edges. (d) Final stage; pores are tetrahedral inclusions at corners where four tetrakaidecahedra meet. [10] 8

Figure 3 : **Early phenomenological models for intermediate stage and final stage of sintering. Pictures in above are packing of spheres. Pictures in below are porous structures.** 10

Figure 4 : Cell construction in the left showing a grain and its associated porosity, at initial stage sintering (after DeHoff'). The shaded areas represent solid contact areas between cells, i.e., grain boundaries. Pyramid subgeometry of a cell is shown in the right side. [28] ... 14

Figure 5 : Basic sintering results from the experiments. Specimens were heated to 1500^{o}C at heating rate of 8, 15, 30 and 45^{o}C/min in oxygen at a pressure of 1.7 Kpa. [30] 17

Figure 6 : **MSC constructed from the sintering data shown in Figure 5 (activation energy used in the calculation was taken as 488 KJ/mol).** [30] 18

Figure 7 : Illustration of agglomerated particles. 20

Figure 8 : Diagrammatic demonstration for the heating procedure used in this experiment. Samples were heated at a rate of 5^{o}C per minute to a target temperature, then were held at the peak temperature for a desired time, finally were cooled down at a rate of 10^{o}C per minute to room temperature. 24

Figure 9 : Showing the density slice operation in which the top line in left toolbar is dragged to adjust the contrast of image when "Density Slice" command was performed. . 31

Figure 10 : The original SEM image (left) and the binary image converted from it by software "ScionImage" (right). [21] 31

Figure 11 : A sample tessellation map. Black areas were pore areas. A cell was consisting with a pore and the area of single color surrounds the pore. 32

Figure 12 : Illustration of tessellation cell properties. CA, SA and PA were defined as in equation 3.9. [21] 33

Figure 13 : A color plot of SAF-CA for a pressed ZrO_2 sample. 34

Figure 14 : A three dimensional illustration of the cell map shown in Figure 13. Height of colorful block shows the frequency of cells with corresponding CA and SAF. 34

Figure 15 : The effect of sintering time on solid volume fraction of ZrO_2-3mol%Y_2O_3. 36

Figure 16 : Comparison of Apparent Densities and Bulk Densities of the Zirconia samples studied here. 38

Figure 17 : The relationship for isothermal sintering of LPLT, HPLT and LPHT between volume strain rate and solid volume fraction. 39

Figure 18 : Illustration of uniform neck growth between two ceramics particles by mechanism such as grain boundary or volume diffusion. [15] 40

Figure 19 : The average grain intercept lengths and pore intercept length plotted against solid volume fraction for LPLT samples. 42

Figure 20 : The average pore separation lengths of LPLT samples plotted against solid volume fraction for LPLT samples. 42

Figure 21 : Plot of ratio of average pore separation intercept length and grain intercept length against solid volume fraction...... 43

Figure 22 : A high magnification SEM image shows there is few pores in triple point on polished cross-section of this zirconia ceramics. 44

Figure 23 : A two dimensional representation of a microstructure with more than one grain between pores. Vacancy annihilation on boundary between grain 1 and grain 2 would create tension without mass transport along boundaries between grain 1 and grain 3 and boundaries between grain 2 and grain 3 in response to stress...... 46

Figure 24 : The number of pores per unit area plotted against solid volume fraction for LPLT samples...... 47

Figure 25 : The effect of sintering time on the pore area distribution by area for samples with a green density of 0.45 sintered at 1275^{O}C...... 48

Figure 26 : The plot of average pore area against sintering time for LPLT samples...... 49

Figure 27 : Frequencies of cell area for cells on a tessellation map of the sample which was held at 1275^{o}C for 5 hours in group LPLT...... 50

Figure 28 : Frequencies of solid area fraction (SAF) for cells on a tessellation map of the sample which was held at 1275^{o}C for 5 hours in group LPLT. 51

Figure 29 : The plot of tessellation cell solid area fraction (SAF) against cell area (CA) for LPLT sample fired for 5 hours. The different colors represent ranges of relative frequency and are used to help show the shape of the distributions. Note that CA is plotted on a logarithmic scale...... 51

Figure 30 : A three dimensional demonstration of the cell map...... 52

Figure 31 : Plots of tessellation cell solid area fraction (SAF) against cell area (CA) for samples fired for 0.5 hours, 1 hour, 5 hours and 10 hours. The different colors represent ranges of relative frequency and are used to help show the shape of the distributions. Note that CA is plotted on a logarithmic scale. 53

Figure 32 : Comparison of ratio of pore separation to grain intercept length between previous studied commercial alumina and the zirconia materials in this study. 55

Figure 33 : The microstructure of a sample sintered for 1 hour at 1275^{O}C showing the wide pore size distribution. 56

Figure 34 : The microstructure of a sample sintered for 5 hour at 1275^{O}C showing the dense areas between the widely spaced pores...... 56

Figure 35 (a), (b): Damages were found in the low magnification SEM image of the polished cross section of HPLT sample sintered for 0.5 hours at 1315^{o}C...... 59

Figure 36 (a), (b): Damages were found in the low magnification SEM image of the polished cross section of HPLT sample sintered for 5 hours at 1275^{o}C...... 60

Figure 37 : Low magnification SEM image of LPLT sample showed there was no large damage on polished cross-section. 61

Figure 38 : The differences between global solid volume fraction and local solid line fraction are plotted against global solid volume fraction for LPLT, LPHT and HPLT samples. 61

Figure 39 : The average intercept lengths plotted against solid volume fraction for the grains. 62

Figure 40 : The average pore intercept lengths plotted against solid volume fraction for the pores. 62

Figure 41 : The average pore intercept lengths plotted against solid line fraction for the pores. 63

Figure 42 : The plot of average pore separation intercepts length against solid volume fraction. 63

Figure 43 : The plot of average pore separation intercepts length against solid line fraction. 64

ACKNOWLEDGEMENTS

I would like to begin to thank my advisor, Professor Ian Nettleship, for his guidance and support throughout my graduate study at the University of Pittsburgh. Prof. Nettleship not only showed me what to do as a scientific professional, also presented me how to live the life as a human being. I would also like to thank precursors of our porous materials laboratory, especially Dr. Richard John McAfee, Jr. My research in this laboratory began from the experimental skills and knowledge taught by him. The members of my thesis committee, Prof. Pradeep P. Fulay and Prof. John P. Leonard, are gratefully acknowledged for their essential technical and philosophical input of this work. The faculty, staff, and students of the Materials Science & Engineering Departments have greatly enriched my experience at the School of Engineering, making past years an enjoyable memory for me. Also, the encouragement and support of my family, especially my husband, Yang Dong, makes me more motivated in pursuing my education. Last but not least, financial support from the Sandia National Laboratory is gratefully acknowledged.

1.0 INTRODUCTION

Sintering commonly refers to processes of consolidating a body shaped from powder particles which involves heat treatment at elevated temperatures, usually at $T > 0.5T_m$ [K] (T_m is the melting temperature for that specific material). Diffusional mass transport is appreciable in this elevated temperature range. Usually a self-supporting compact is obtained by pressing, casting or other processing before sintering. Almost all aspects of the sintering process have been addressed in many books and publications. [1, 2, 3, 4, 5]

Polycrystalline ceramic material is one very common category which would receive sintering treating. Ceramic processing is based on the sintering of powder compacts rather than melting, forging or other methods. The reasons for that are addressed below. First, ceramics usually melt at high temperatures, which makes melting difficult and inefficient. Second, ceramics are brittle which is not suitable for processing by thermo-mechanical forming. While sintering of ceramic materials has been practiced since the beginning of human civilization the process is still not understood to the point that the effects on shrinkage and microstructure can be accurately predicted.

In response to the inability of the early phenomenological models to predict sintering shrinkage and shape change under most practical circumstances, attention was paid to continuum modeling. The continuum models that have been developed for the prediction of shrinkage have been comprehensively reviewed by Olevsky.[6] Examples include viscoplastic approaches, such as

that of Besson and Abouaf [7] and the more common viscous models, such as that of Scherer and Bordia.[8] Often, the only microstructural variable in these models is density or solid volume fraction. However, the phenomenological contact flattening models [9, 10] can be used for time and temperature compensation in the continuum model. Unfortunately, the large number of material constants and variables required leads to a situation wherein material data such as activation energies become adjustable parameters in a curve fitting exercise.[11] To a certain extent, this can be mitigated by calibration of material properties, such as uniaxial viscosity, in thermal treatments that faithfully reproduce aspects of the sintering cycle.[12, 13] While the continuum approach has provided a very practical method for predicting sintering shrinkage, it is not capable of direct representation of internal variables, such as particle packing arrangement, particle rearrangement, and grain growth, that are known to affect the final density and the microstructural evolution. In response to this problem, there is now another shift about to take place in the modeling to three-dimensional mesoscale microstructural simulation of sintering.[14]

The study addressed in this thesis started from the basic single phase sintering using zirconia nanocrystalline power. The goal is to characterize the microstructure of the materials during isothermal sintering and to provide a better understanding of powder processing effects for aggregated nanocrystallize powders. This information will be required to implement the new numerical simulations.

2.0 BACKGROUND

2.1 SINTERING

2.1.1 Driving force of sintering

The driving force for densification and coarsening during sintering is the decrease in the surface free energy of power compacts. Since Γ_{SV} (surface free energy at solid-vapor interface) is normally greater than Γ_{SS} (surface free energy at solid-solid interface), the solid-vapor interfaces tend to be replaced by solid-solid interfaces when enough energy is provided. This mechanism is illustrated by **Figure 1**. The two spheres model is commonly used for the initial stage of sintering. The intermediate stage and final stage of sintering use different geometrical models while the driving forces and diffusion mechanisms are the same.

The starting point for predicting shrinkage is usually the Gibbs-Thompson-Freundlich equation which is shown below, which describes the difference in equilibrium concentration of vacancies for a curved surface (c) relative to a flat surface (infinite curvature, c_0), [15]

$$c = c_0 \exp\left[\frac{\gamma V_m}{RT}\left(\frac{1}{r_1}+\frac{1}{r_2}\right)\right] \qquad \text{Equation (2.1)}$$

Where r_1 and r_2 are the principle radii of curvature for the curved surface, V_m is the molar volume, γ is the energy per unit area of the surface, R is the gas constant, and T is the absolute temperature. The radii of curvature for a convex surface, such as the particle surface, are

positive. However, in the concave neck region the radius in the plane of the contact area between the particles will be positive but the radius in the plane of the particle centers will be negative. In **Figure 1** which illustrates neck growth between two particles, the radius of particles a is positive and the radius of the neck r is negative, which results in a greater vacancy concentrations under the surface of the neck. Thus mass is driven to transport toward the surface of the neck from the convex surface or from the grain boundary.

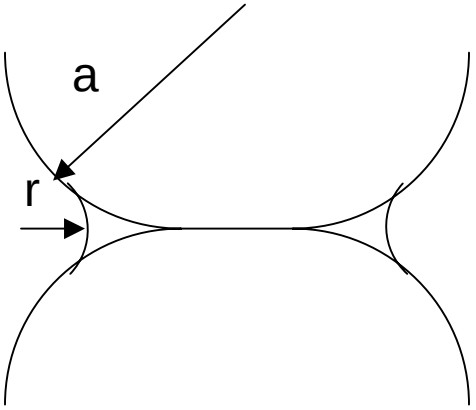

Figure 1 : **Illustration of the two-sphere sintering model geometry. The neck radius is given by r and the particle radius is a.**

2.1.2 Flux of atoms

Diffusion is among the most important phenomena observed in ceramic materials. The diffusion of atoms is generally necessary for changes in microstructure to take place in processes such as the densification of powder compacts, creep deformation at high temperatures, grain growth, and the formation of solid-state reaction products and solid ionic conductors. Atomic diffusion rate is largely dependent on the type of defects present and their concentrations.

Diffusive mass transport takes place when there is a gradient in the chemical potential and when the species in question has sufficient mobility. In continuum diffusion, transport is described by solutions to Fick's first and second laws, under geometric and concentration

boundary conditions, which are determined by the experimental configuration. Fick's first law (in one dimension):

$$J = -D\left(\frac{dC}{dx}\right) \qquad \text{Equation (2.2)}$$

states that the atom flux J (number per unit area per unit time) at a steady state is proportional to the concentration gradient dC/dx. The proportionality constant D is termed the diffusion coefficient or diffusivity, and is usually written in units of cm^2/sec.

Fick's second law describes the accumulation or depletion of concentration, C, when steady-state conditions are not achieved, and is obtained from the spatial derivative of the flux:

$$\frac{\partial C}{\partial t} = -\frac{\partial J}{\partial x} = D\left(\frac{\partial^2 C}{\partial x^2}\right) \qquad \text{Equation (2.3)}$$

The diffusional flux of atoms at neck, j_a, during sintering of a pure compound is governs by Herring's equation,[16] the general flux equation, which is shown below,

$$j_a = -\frac{D}{\Omega_a K_B T}\nabla(\mu_a - \mu_V) \qquad \text{Equation (2.4)}$$

where μ_a and μ_v are the chemical potentials of the atoms and vacancies, respectively, $\nabla(\mu_a - \mu_v)$ is the chemical potential gradient related to curvature which drives mass transport, D/k_BT represents the mobility term for either grain-boundary or volume diffusion, k_B is Boltzmann's constant, D is the diffusivity, T is absolute temperature, and Ω_a is the atomic volume.

There are a number of competing paths for mass transport during ceramic sintering, such as grain boundary diffusion, volume diffusion and surface diffusion. Some of these, usually surface diffusion, leads to coarsening, which is a growth of the neck between particles leading to reduction of the specific surface area without approach of particle centers. Other transport

mechanisms, normally volume diffusion and grain boundary diffusion lead to densification, which is defined as neck growth with approach of particle centers. In densification mechanisms (in the absence of viscous flow and plastic deformation), the grain boundary plane serves as the "source" for diffusional transport, and the neck as the "sink" or repository for atoms.

Zirconia containing 3 mol% ytrria was studied in this research. Defect equation in this ceramic material is listed below:

$$Y_2O_3 \xrightarrow{ZrO_2} 2Y'_{Zr} + 3O_O^X + V_O^{\bullet\bullet} \qquad \text{Equation (2.5)}$$

The diffusion species seems to be O^{2-} according to the defect equation. However, since in both tetragonal zirconia and cubic stabilized zirconia, $D_O^l >> D_{Zr}^l$, oxygen will not control the rate of sintering. In fact a complex diffusion coefficient D_{comp} must be defined to avoid demising of the oxide. $D_{comp} = D_{Zr}^l + (\pi / d)\delta D_{Zr}^b$, where D_O^l and D_{Zr}^l are the oxygen and zirconium lattice diffusion coefficients, respectively, D_{comp} is the complex diffusion coefficient, D_{Zr}^b is the zirconium boundary diffusion coefficient, d is the grain size and δ is the boundary width. Okamoto *et al* calculated the D_{comp} for this yttria doped zirconia material [17] from the creep data and the equation [18] litsed below.

$$\dot{\varepsilon} = \frac{14\sigma\Omega D_{comp}}{d^2 kT} \qquad \text{Equation (2.6)}$$

where $\dot{\varepsilon}$ is the strain rate, σ is the stress, Ω is the molecular volume, d is the grain size, T is the absolute temperature, and k is the Boltzmann's constant. Their results were comparable with the interdiffusion coefficient for Zr-Hf in cubic zirconia, [19] suggesting that $D_{comp} \approx D_{Zr}^l$. Thus, it has been argued that in this Y_2O_3 stabilized cubic zirconia material, the mass

transportation is controlled by the cation lattice diffusion. In summary, the diffusion species in this material is Zr^{2+}, not O^{2-}.

2.1.3 Sintering stages

Classically, the process of sintering is arbitrarily divided into three stages, the initial, intermediate, and final stages based on physical reasoning so as to arise at simple geometries for densification by contact flattening**. Figure 2** demonstrated the model geometry of the three stages of sintering, which have been chosen to simplify the problem of developing closed form solutions for densification based on the flux equations.

(a) The initial stage of sintering

At the initial stage of sintering, powder particles are assumed to deform and the contact points between particles flatten to form necks without significant densification. The surface of necks forms saddles with negative curvature. Usually initial stage sintering is considered to be complete after, at most 10% densification. This usually occurs in the early stages of heating in most practical applications of sintering. For example, the green densities of samples in this study were 0.45 and 0.51. Therefore, using the above criteria, the end of initial stage of sintering would have been reached when the solid volume fraction of those samples reached values of 0.55 and 0.61 which were reached, during heating, well before the isothermal sintering temperature was reached. Since the solid-vapor interface area is large at the beginning of sintering, the driving force for sintering is also large, and initial stage of sintering will be complete in seconds or minutes when subject to a high temperature environment. The zirconia materials used in this study achieved at least 25% densification after heating and being held at the target temperature

for 6 minutes. It can therefore be concluded that isothermal experiments in most circumstance will not examine initial stage sintering.

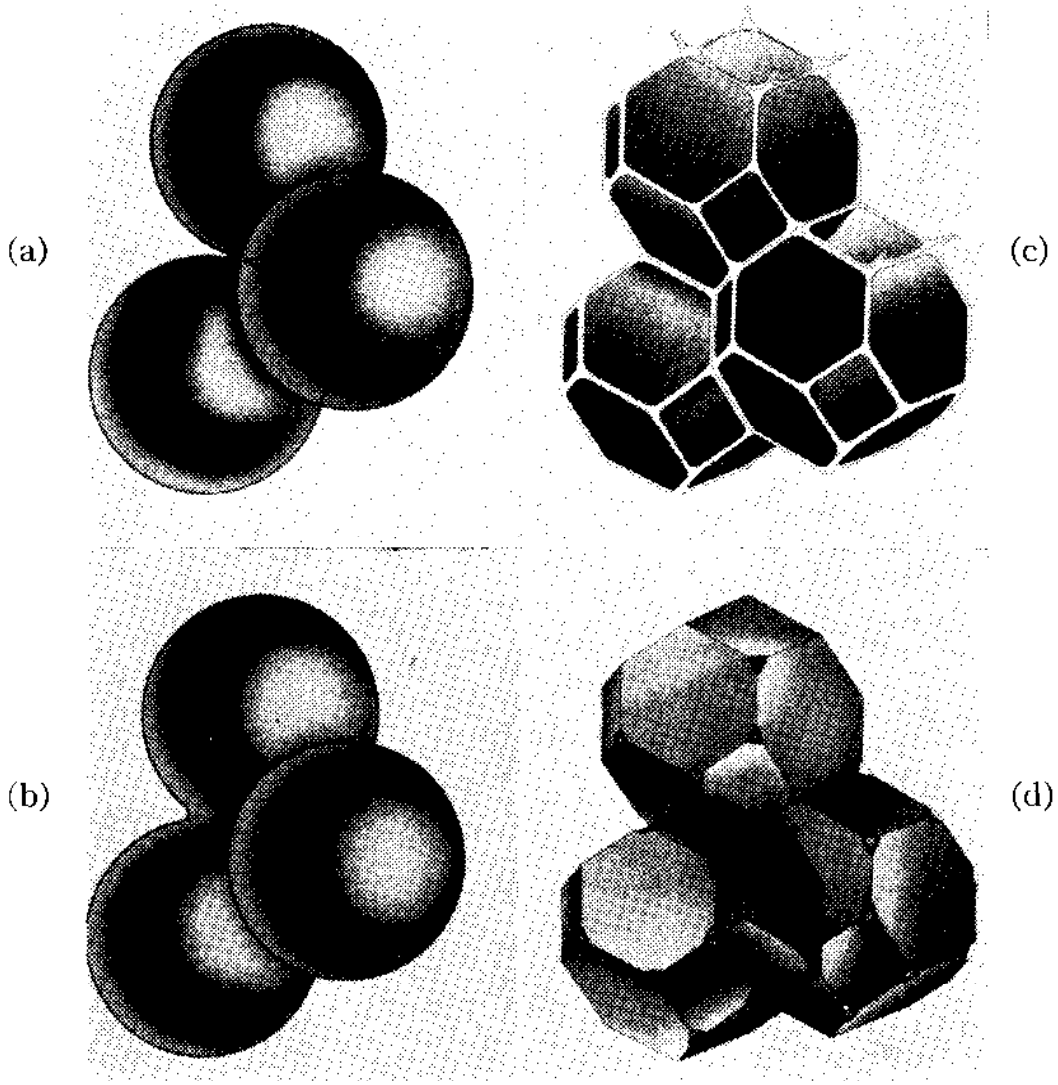

Figure 2 : (a) Initial stage of sintering; model structure represented by spheres in tangential contact. (b) Near end of initial stage. Spheres have begun to coalesce. The neck growth illustrated is for center-center shrinkage of 4%. (c) Intermediate stage; dark grain have adopted shape of tetrakaidecahedron, enclosing white pore channels at grain edges. (d) Final stage; pores are tetrahedral inclusions at corners where four tetrakaidecahedra meet. [10]

(b) Intermediate stage of sintering

During the intermediate stage of sintering, neck growth occurs and interconnected porous channels are formed. The microstructure evolves into a complex structure of interpenetrating

networks of grains and pores. The compact shrinks and densifies up to a value above 0.9 in solid volume fraction. As the particles contact, they continue to flatten allowing the particles centers to approach. Besides shrinkage, another phenomenon called grain growth or coarsening happens if the material transport mechanism originates on the surface of particles and no compact shrinkage occurs. In such cases, particle faceting becomes less prominent at higher temperatures compared with its faceting at lower temperatures.[20] Coarsening reduces the surface energy of the system and decreases the driving force for densification. Thus, in isothermal sintering, the densification rate decreases as the neck sizes increase. In most case, grain growth and grain coarsening are not desirable. High density and fine grains of ceramics are the goals of most studies. For systems that densify well there tends to be little grain growth in intermediate sintering due to pinning of grain boundaries by a uniform distribution of fine pores.

(c) Final stage of sintering

After sintering reaches the final stage, pores become isolated and the solid volume fraction of materials exceeds about 0.92. Ideally, at the end of the final stage of sintering, all pores are eliminated and materials are 100% dense. However, there are commonly randomly distributed residual pores present in the material.

It must be stated at this point that these description of the stages of sintering are qualitative and broad and fail to capture the real complexity of microstructure evolution. Their main purpose has been to highlight the main issues and provide the foundation for phenomenological modeling.

2.1.4 Traditional model of single-phase sintering and predictive capability

Simple geometries have been used to model the microstructure evolution during the stages of sintering. As shown in **Figure 3**, in early phenomenological models the microstructure of initial stage models were commonly represented by ordered arrays of spheres. In contrast, intermediate stage and final stage of sintering are based on space filling body tetrakaidecahedrons. The difference between latter two stages is the pores are interconnected

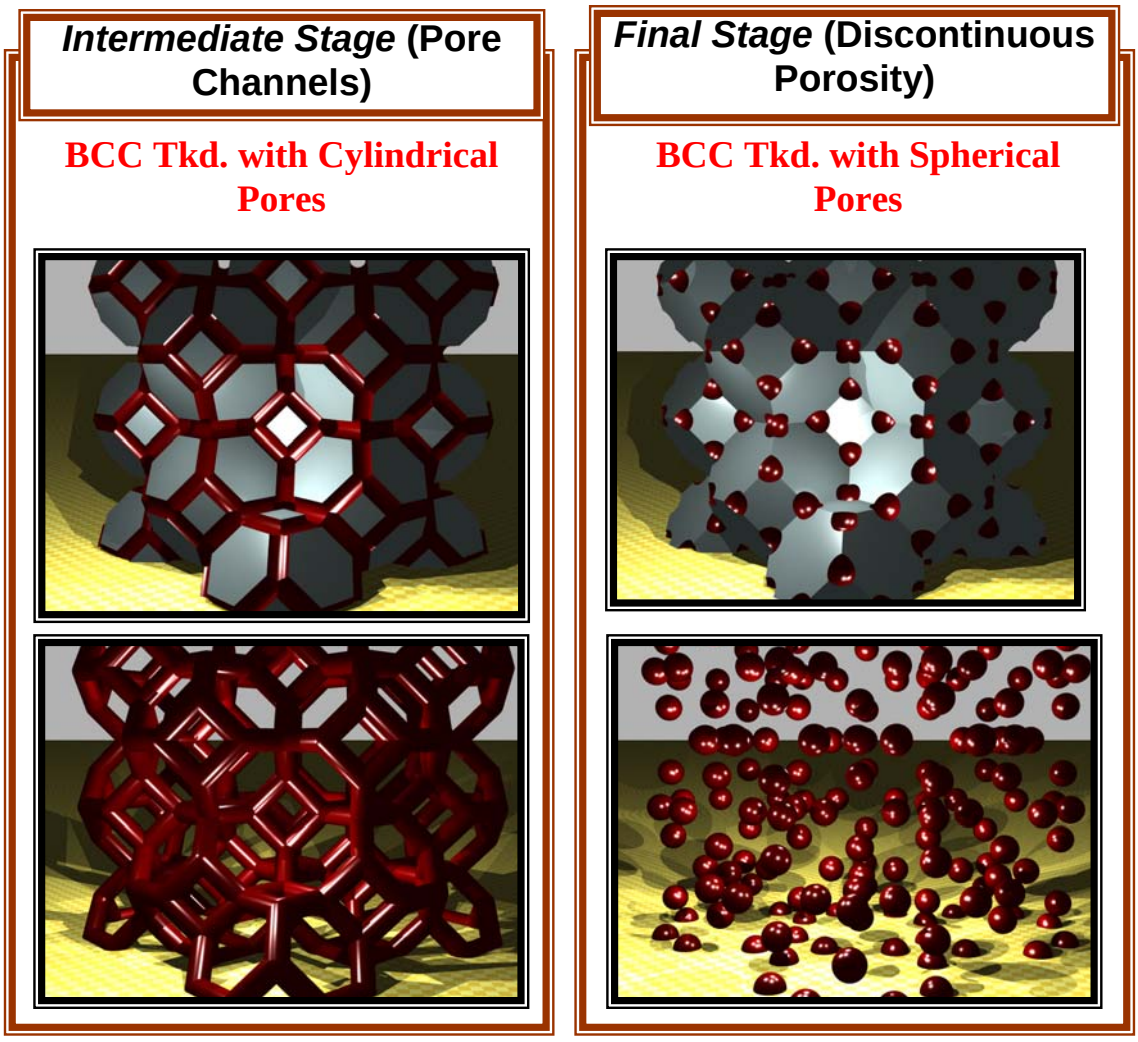

Figure 3 : **Early phenomenological models for intermediate stage and final stage of sintering. Pictures in above are packing of spheres. Pictures in below are porous structures.**[21]

cylindrical channel located on the 36 edges of the retrakaidecahedrons for intermediate stage. While in the model for the final stage of sintering, pores are spheres located on all 24 corners.

In these early models, the geometries allow uniform shrinkage as densification proceeds and the distance between particle centers decreases and flat contacts between the particles grow. The ways in which the contacts impinge upon each other determine the ranges of solid volume fraction over which these models can be applied. For example, if spheres are packed in a simple cubic arrangement, the solid volume fraction ranges from approximately 0.52 (point contact between particles) to 0.82 (contact between necks, which would form a new grain edge and break the geometrical constraints of the model). If spheres are face centered cubic packed, the solid volume fraction may range from 0.72 (by pore to pore contact) to full density. Obviously, perfect packing can not be achieved in real materials due to non-uniform packing and irregular shaped particles. Another example of a constraint is the low solid volume fraction limit for the initial stage model when the pores impinge along grain edges.

Other initial stage geometries such as dense random packing[22] can also be found in the literature. But common to all these traditional sintering models is the requirement that the problem of representing sintering microstructures can be reduced to a representative volume containing a single particle and its attendant porosity. That is to say, the diffusion length is determined by the particle size or grain size and that the grain size can scale the shrinkage of a ceramic on sintering to the diffusion length.[23] But if compacts were formed by non-equal sized particles or irregular packing, the real microstructures can not be well represented. Thus a means of imposing a distribution of particle or pore size can not be provided by these models because of the geometric constraints. Similarly the models can not implicitly address different particle packing arrangements and the consequent of effect of green density.

The models are not directly capable of representing grain growth or coarsening. If the geometrical constraints are to be represented only a self similar scaling of the microstructure can occur. Nettleship *et al* reported that nondimensional parameters can be used to make direct comparisons of coarsening to densification models with experiments, independent of scale.[24] As defined in equations (2.7) and (2.8), the two nondimensional parameters used are the surface area ratio (ψ), which is the ratio of the surface areas of solid/solid and solid/vapor boundaries, and the intercept ratio (Λ), which is the ratio of mean grain and pore intercept lengths.

$$\psi = \frac{S_V^{SS}}{S_V^{SV}} \qquad \text{Equation (2.7)}$$

$$\Lambda = \frac{\lambda_g}{\lambda_p} \qquad \text{Equation (2.8)}$$

The predicted evolutions of these parameters during densification in the simple geometric models have been previously determined.[25] Because ψ and Λ are independent of the length scale of the microstructure, their value are unaffected by self-similar coarsening from the fixed microstructural geometry assumed in the models. ψ is better than Λ for final stage sintering because of the assumption that all pores are on grain boundaries in the definition of λg. The final stage sintering model commonly underestimates ψ, this can be attributed to the pores in the model being too small relative to the grains and therefore some grain edges and grain corners do not contain pores in the real materials.

Unlike the phenomenological models, which only allow densification, Weiser and De Jonghe observed regions of de-densification in real microstructures in which some necks are broken to facilitate the rearrangement of particles.[26] The processes of particle rearrangement are not addressed in the commonly used phenomenological models. It was concluded that the non-uniform arrangement at particles in real sintering microstructures result in particle rearrangement

by differential densification, local densification or de-densification. However the phenomenological models continue to be applied to predictions of the effect of porosity on mechanical properties in addition to densification kinetics based on contact areas.[27] While there is some success in predicting densification kinetics, the limited representation of microstructure evolution may inhibit the widespread use of these models in manufacturing.

2.2 THE MASTER SINTERING CURVE

One of the most successful applications of the phenomenological models is the master sintering curve and its use to predict the effect of time and temperature on sintered density. This is based on the combined stage sintering model.

2.2.1 Combined-stage sintering model

Hansen *et al* derived a single equation that quantifies sintering as a continuous process from the beginning to end by focusing on the similarities between the three stages of sintering.[28] Details have been provided by Hansen *et al* in the same paper.

The equation was derived from Herring's equation in equation (2.9),

$$j_a = -\frac{D}{\Omega_a K_B T}\nabla(\mu_a - \mu_V) \qquad \text{Equation (2.9)}$$

The chemical potential gradient at the pore surface will be proportional to the curvature, K, and inversely proportional to the distance over which material is drawn to the pore, λ. The

scaling parameters which relate these terms to the particle or grain diameter, G, are assumed by the following relationships:

$$K = -\frac{C_k}{G} \qquad \text{Equation (2.10)}$$

$$\lambda = C_\lambda G \qquad \text{Equation (2.11)}$$

where the curvature of pore is taken as negative.

When applied to the DeHoff cell model, (shown in **Figure 4**) atomic flux will result in shrinkage of the centroid-base distance by dh_p and expansion of the grain-boundary area of the pyramid S_p^b (see **Figure 4**). Although S^b and h are not known for a general microstructure, they are assumed to scale with grain size as

$$S^b = C_a G^2 \qquad \text{Equation (2.12)}$$

$$h = C_h G \qquad \text{Equation (2.13)}$$

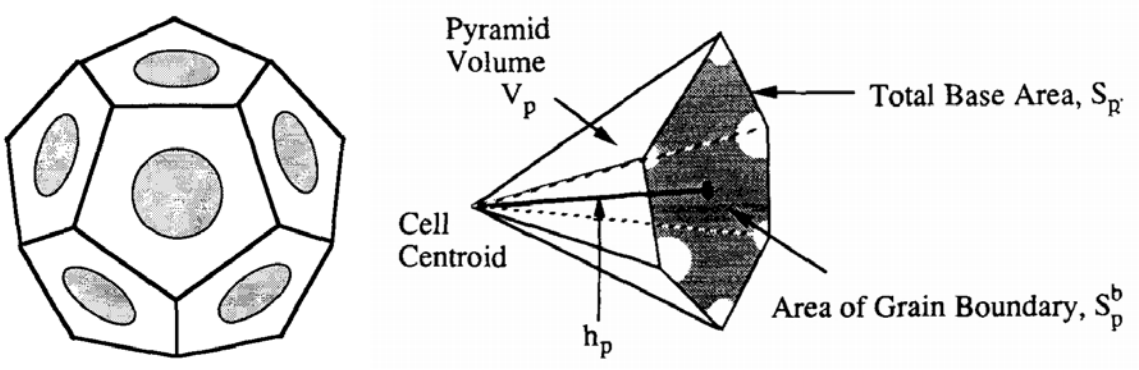

Figure 4 : Cell construction in the left showing a grain and its associated porosity, at initial stage sintering (after DeHoff' [29]). The shaded areas represent solid contact areas between cells, i.e., grain boundaries. Pyramid subgeometry of a cell is shown in the right side.

Thus, the overall isotropic shrinkage of a material that can be represented by the DeHoff cell model is

$$-\frac{dL}{Ldt}=\frac{\gamma\Omega}{kT}\left(\frac{\Gamma_v D_v}{G^3}+\frac{\Gamma_b \delta D_b}{G^4}\right) \qquad \text{Equation (2.14)}$$

where γ is the surface energy, k_B is Boltzmann's constant, D is the diffusivity, T is absolute temperature, and Ω_a is the atomic volume, G is the mean grain diameter.

The dimensionless geometric parameter Γ comprises five scaling factors that relate specific microstructural feature to the scale (grain diameter). They lump the assumed dependencies of driving force and flux to the scale of the microstructure (grain size). Therefore equation (2.14) relates the instantaneous linear shrinkage rate to the diffusion coefficient and other material parameters and mean grain diameter. This is the basis of the master sintering curve approach.

$$\Gamma_b=\frac{aC_kC_b}{C_\lambda C_a C_h} \qquad \text{Equation (2.15)}$$

$$\Gamma_v=\frac{aC_kC_v}{C_\lambda C_a C_h} \qquad \text{Equation (2.16)}$$

2.2.2 The master sintering curve (MSC)

The MSC [30] predicts densification results under different thermal histories for a given green processing method. It is based on the combined-stage sintering model therefore avoid the geometrical discontinuities between the stages of sintering provided that one diffusion mechanism dominates in the sintering process.

The master sintering curve characterizes the sintering behavior for a given powder and green body process regardless of the heating profile. Although the concept of the MSC is general, its formulation and construction can be derived from Equation (2.14)

For isotropic shrinkage, the linear shrinkage rate can be converted to the densification rate by assuming densification is isotropic

$$-\frac{dL}{Ldt}=\frac{d\rho}{3\rho dt} \qquad \text{Equation (2.17)}$$

where ρ is the bulk density (or relative density). If there exists only one dominant mechanism during the sintering, and assuming that Γ and G are functions of only density, equation (2.14) can be simplified and rearranged to

$$\int_{\rho_0}^{\rho}\frac{(G(\rho))^n}{3\rho\Gamma(\rho)}d\rho=\int_0^t\frac{\gamma\Omega D_0}{kT}\exp\left(-\frac{Q}{RT}\right)dt \qquad \text{Equation (2.18)}$$

where Q is the apparent activation energy, R is the gas constant For volume diffusion, $D_0=(D_v)_0$ and n=3,; for grain-boundary diffusion, $D_0=(\delta D_b)_0$ and n=4. ρ_0 is the green density of the powder compact.

Defining Φ(ρ) to incorporate both microstructural scale, G(ρ), and scaling parameter Γ(ρ),

$$\Phi(\rho)\equiv\frac{k}{\gamma\Omega D_o}\int_{\rho_o}^{\rho}\frac{(G(\rho))^n}{3\rho\Gamma(\rho)}d\rho \qquad \text{Equation (2.19)}$$

Similarly Θ(t, T(t)) can be defined to include all varieties of sintering history in Equation (2.14),

$$\Theta(t,T(t))\equiv\int_0^t\frac{1}{T}\exp(-\frac{Q}{RT})dt \qquad \text{Equation (2.20)}$$

Θ (t, T (t)) depends only on Q and the time-temperature profile. Thus,

$$\Phi(\rho)=\Theta(t,T(t)) \qquad \text{Equation (2.21)}$$

Φ(ρ) is considered a characteristic function that quantifies the effects of the microstructural evolution on the kinetics as densification occurs. The relationship between ρ and

$\Phi(\rho)$ is defined as the master sintering curve. However it is difficult to evaluate because of the need for independent measurements of $G(\rho)$ and $\Gamma(\rho)$. Therefore, constant heating rate sintering experiments are usually performed at a variety of rates to evaluate $\Theta(t, T(t))$ which is then used with the activation energy to define the master sintering curve based on equation (2.21).

The example of master sintering curve is provided by H. Su and D. L. Johnson. In their experiment, a set of commercial alumina specimens first were rapidly heated at 1°C/s to 750°C and then to 1500°C at constant heating rate of 8, 15, 30 and 45°C/min in a high-purity oxygen atmosphere at a pressure of 1.7 Kpa. The sintering result plotted in **Figure 5** where shown to collapse on to a single $\Theta(t, T(t))$ relationship as required by the MSC as shown in **Figure 6**.

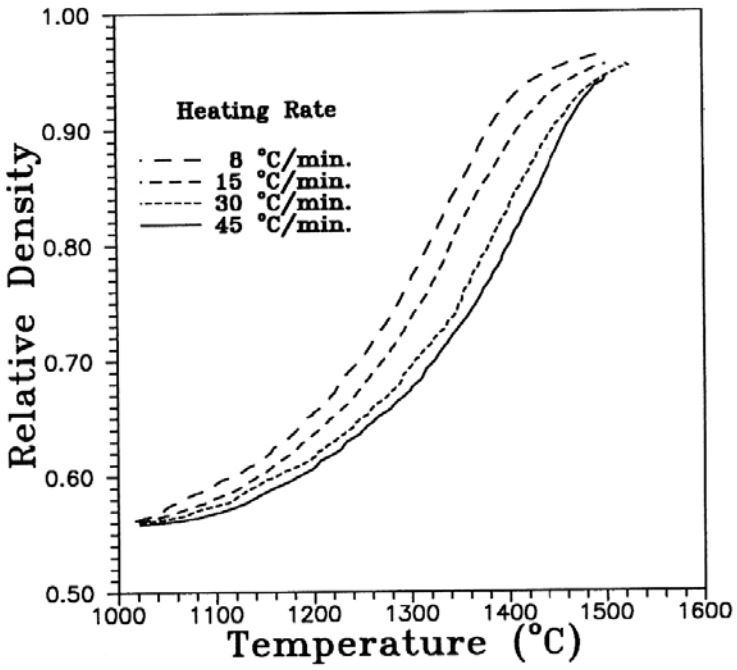

Figure 5 : Basic sintering results from the experiments. Specimens were heated to 1500°C at heating rate of 8, 15, 30 and 45°C/min in oxygen at a pressure of 1.7 Kpa.

The master sintering curve has proven to be an effective tool to predict the effect of temperature and time on sintered density.[31] However, it is restricted to isotropic shrinkage for constant green microstructures and therefore is unable to make a prediction when the green

processing method or the original power is changed. This limits its use to manufacturers who make a variety of shapes from the same material. The model also assumes that the evolution of the microstructure represented by G(ρ) is independent of thermal history.

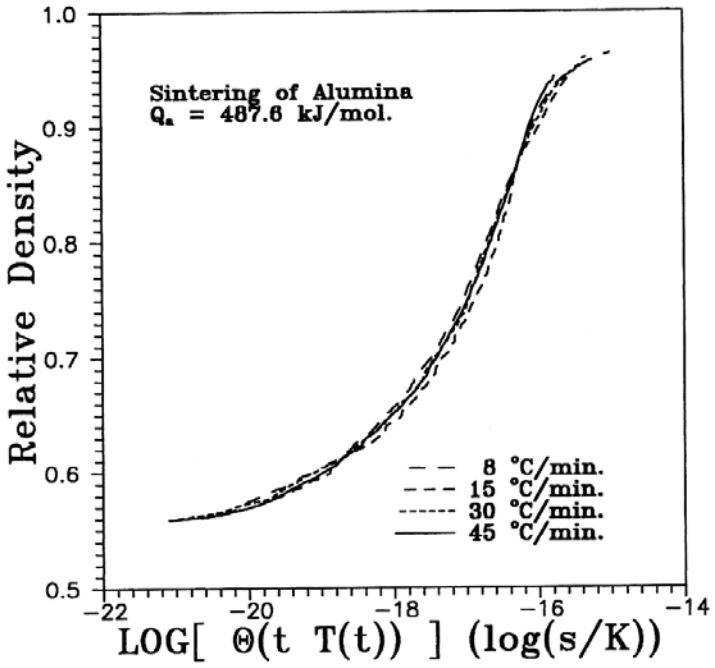

Figure 6 : MSC constructed from the sintering data shown in Figure 5 (activation energy used in the calculation was taken as 488 KJ/mol).

2.3 EFFECT OF POWDER PROCESSING VARIABLES

For the purpose of this study, to widen the applicability of the MSC approach, it will be important to understand how microstructural evolution affects the suitability of the assumptions. A distinction will be made between the densification and microstructure evolution of micron size powders that tend to be monocrystalline and nanocrystalline powders that tend to be aggregated.

It is now well know that there are intrinsic effects of sizes on the properties of nano-particles that go beyond those that can be predicted by scaling down macroscopic properties.

These effects are usually explained by the effect of finite size on the atomic potentials of atoms. For example, there have been reports focusing on the dependence of melting points on the size of small crystallites. For example, Buffat et al. have studied size effect on the melting temperature of gold particles [32] and Coombes has studied the melting of small crystallites of lead, indium and bismuth. [33] They all observed a depression in melting point inversely proportional to the particle diameter. However, this size effect only becomes clearly visible when particle diameter is smaller than 10 nm. The average diameter of the zicronia particles used in this study is 28 nanometers, which suggests that those samples are not expected to such deviations from bulk behaviors.

2.3.1 Effects of powder processing on green density

The green densities of most ceramic compacts are well below even dense packing of equsized spheres. The particles tend to agglomerate or clump, as showed in **Figure 7**, smaller voids exist inside agglomerates and larger porous space existed between the agglomerates. This agglomeration is due to the Van der Waals force of attraction and condensed moisture of particle contacts which tend to be stronger than gravitational forces that pull the particles apart. Therefore during in processing steps such as powder pressing, pressure is applied, which causes the particle agglomerates to rearrange and reduce the inter-agglomerate pore volume. Inter-agglomerate voids shrink easily under pressure compared with void inside of agglomerates. This leads to a well documented effect of pressing pressure on green density. Colloidal processing can avoid the formation of the large agglomerates that necessarily occurs in powder pressing. However the agglomeration condition is very sensitive to the dispersion condition in the slip.

Flocculation usually causes the formation of particle agglomerates that lower the green density of the ceramic.

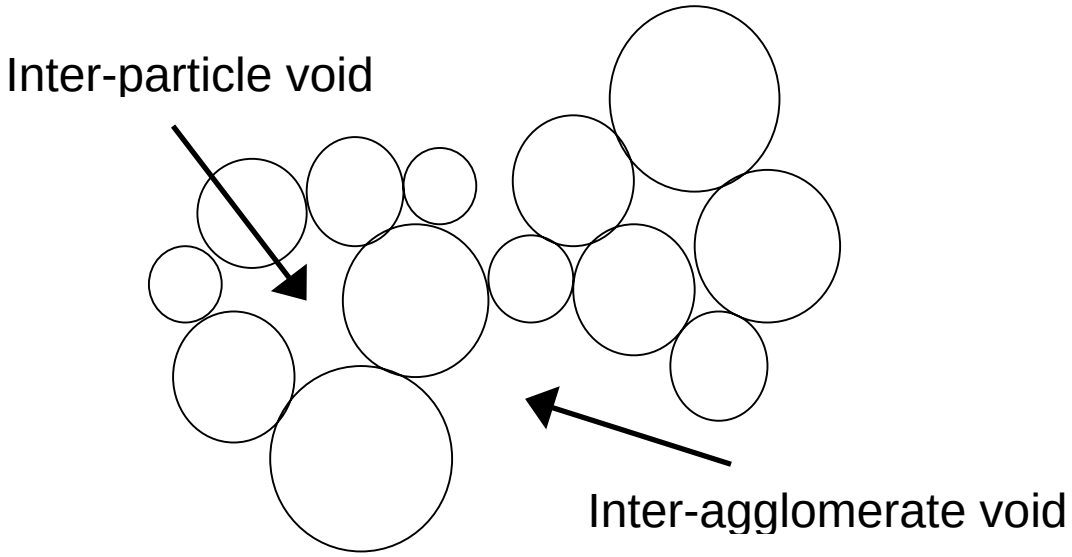

Figure 7 : Illustration of agglomerated particles.

i) Micron size powders

The packing behaviors of micron size powders can be different when produced by different forming methods. Both changing the dispersion condition during slip casting and pressing pressure for granulates powders can vary the green density of compacts. Zheng *et al* made a distinction between these two methods.[34] They suggested that pressed granulated powders result in bimodal pore population with the larger mode being the intergranular pores, which diminish as the pressure increases. While in slip casting, the pore distributed unimodally in a wider range due to the lowing green density caused by flocculation

ii) Aggregated nanocrystallize powders

The inter-particle force inside of agglomerates is much larger than inter-agglomerate force for aggregated nanocrystallize powders. Thus the green density can be very low (50%) due to heterogeneous packing. As pressure applied on green body increases, inter-agglomerate spaces

shrink or are being filled. Thus, compared with compacts formed by micron size powers, the green density of compacts formed by aggregated nanocrystalline powers ranges over a greater span if various pressures are used. However, the final-stage sintering of compacts pressed by nanocrystalline powers is always companied by rapid grain growth.

2.3.2 Effects on densification and microstructure evolution

The size of particles and the particle packing can affect densification and microstructure evolution dramatically. Separately discussion of micron size power and nano-size power will be used here.

i)Micron size powders

Since agglomerate effect is not significant for micron size powders, the whole green body densifies in a relatively synchronized fashion leads to narrow pore size distribution which delays grain growth in final stage sintering. That is to say, as the sintering processes, shrinkage and elimination of pores occur at all area of compacts simultaneously. However, differences in packing behavior have been shown to affect both densification behavior and the onset of grain growth in intermediate stage sintering. For pressed pieces the small inter-agglomerate pores have been shown to control densification rate and shrinkage while the relatively inactive large inter-granule flaws affect final solid volume fraction.[35] While changes in pressing pressure can affect green density, the densification behavior and the grain growth.[36] For slip casting the slip dispersion has been found to affect green density, densification behavior and green growth. Full dispersion gives the best densification and the lowest grain growth.[37]

ii) Aggregated nanocrystallize powders

Small pores inside of aggregated nanocrystallize powders are easily eliminated during the initial stage of densification. On the other hand, spaces between agglomerates are not eliminated at the same rate. Thus, as sintering processes, some high density areas are formed in a matrix of lower density materials, which can support grain growth. The role of pore elimination in this has not been fully investigated. This behavior has lead to a very strong correlation between grain growth and densification for nano-crystalline ceramic powders. Li *et al* examined the properties of ceramic pressed by a nano-crystalline alumina powders with a mean particle size of about 10 nanometers. They found that the relative densities of the green compacts and the sintered Al_2O_3 nano-ceramics rapidly increase with increasing compaction pressure on the green compacts. Also, the relative density and average grain size of the Al_2O_3 nano-ceramics increase with increasing sintering temperature.[38] One significant development in this area is the use of a two step sintering cycle to suppress grain growth and result in bulk ceramics with grain size of 50nm. Wang *et al* and Li *et al* prepared Y_2O_3 and Al_2O_3 nano-grain ceramics, respectively, with no grain growth after the second step sintering. [38, 39] This provides a solution to controlling grain growth but is contrary to a basic assumption of the master sintering curve that $G(\rho)$ is independent of thermal history.

3.0 EXPERIMENTAL PROCURE

3.1 SAMPLE PREPARATION

TZ-3YB (ZrO_2-3mol%Y_2O_3 powder with binder from Tosoh Corporation, Japan) was the sample studied in this work. Three sets of TZ-3YB were fabricated under different pressing pressures and sintering temperatures in order to study correlation between sample microstructures and processing conditions. They were labeled as Set LPLT (samples pressed at 51 MPa and sintered at 1275ºC for different times.), Set HPLT (samples pressed at 238 MPa and sintered at 1275ºC for different times) and Set LPHT (samples pressed at 51 MPa and sintered at 1315ºC for different times) respectively.

3.1.1 Preparation of green bodies

TZ-3YB powders were pressed uniaxially in a 12.9 mm diameter die using a hydraulic laboratory press (Model C-Carver Laboratory Press, Fred S. Carver Inc.). A mixture of stearic acid and ethyl alcohol was coated on the inner surface of die wall as a lubricant. Each sample was pressed from powder weighted about 3 grams. Samples in Set LPLT, HPLT and LPHT were pressed using loads of 51, 238 and 51 MPa respectively. Six disks were fabricated for set LPLT while five disks were made for set HPLT and LPHT. The bulk density of green bodies was calculated as $\rho = M / V$, where M is the mass and V is the volume.

3.1.2 Sintering

A Lindberg Model 51314 box furnace was used to perform sintering. Green disks were placed on a bed of TZ-3YB powder in a covered alumina crucible (McDanel Refractory Company), which was then placed in the center of the furnace. A typical temperature ramp for sintering is shown in **Figure 8**. A heating ramp rate of 5ºC per minute and a maximum cooling rate of 10ºC per minute were used for all samples during sintering. The peak temperatures for samples in Set LPLT, HPLT and LPHT were 1275, 1275 and 1315ºC respectively. Five samples in each set were held at the peak temperature for 0.1, 0.5, 1, 5, 10 hours respectively. The sixth sample in the set LPLT was held at the peak temperature for 50 hours. After sintering, the density of sintered disks was measured based on Archimedes' principle (see Section **3.1.1**).

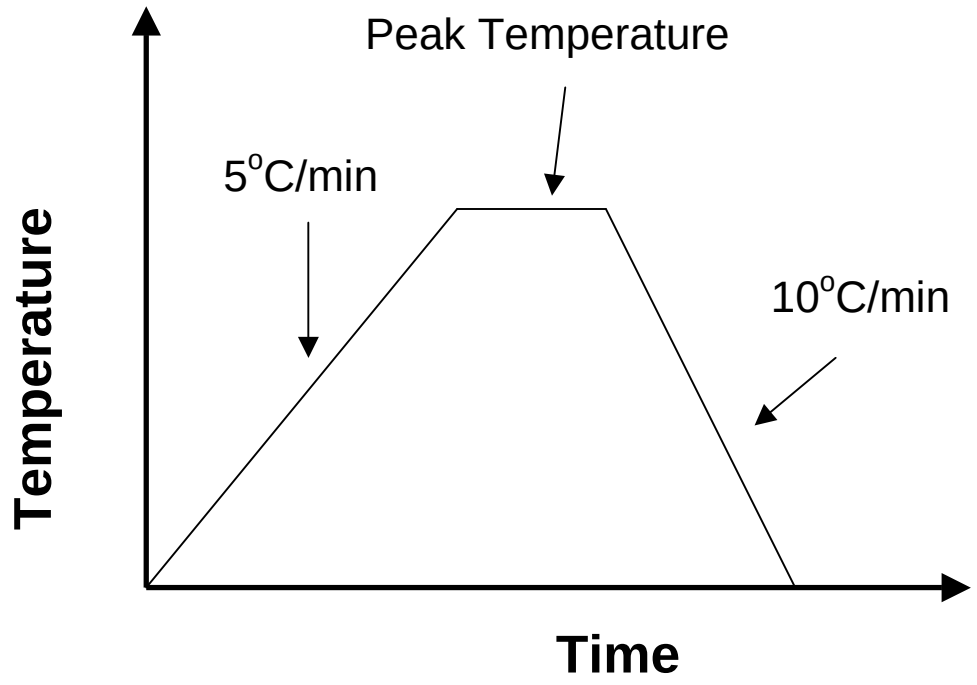

Figure 8 : Diagrammatic demonstration for the heating procedure used in this experiment. Samples were heated at a rate of 5°C per minute to a target temperature, then were held at the peak temperature for a desired time, finally were cooled down at a rate of 10°C per minute to room temperature.

3.1.3 Sample section and preparation for polishing

Each sintered sample was sectioned into two parts with a diamond saw (Isomet Plus Precision Saw. Buehler Ltd.) in order to expose an inner cross section of samples. After the section, samples were vacuum impregnated with a mixture of resin and hardener (Epo-Thin Low Viscosity Epoxy Resin, Epo-Thin Low Viscosity Epoxy Hardener, Buehler Ltd.) into cold mounting cups to prevent pull-out during grinding and polishing.

3.1.4 Grinding and polishing

The sectioned surfaces were ground by a Buehler Ecomet 4 Grinder-Polisher plus Automet 2 Power Head with diamond wheels of 75 μm and 30 μm before they were polished by the same system with Metadi II Diamond Polishing Compound (Buehler Ltd., 15, 6, and 1 μm diameter diamonds were used). A load of 18 lbs and a speed of 70 rpm were used for the grinding process and the first polishing process with 15 μm diameter diamonds. A reduced load of 17 lbs and speed of 50 rpm were used for the following polishing processes using 6 and 1 μm diameter diamonds. Between different polishing steps, samples were immersed in water and washed in an ultrasonic bath (Branson 5200 Ultrasound). After all grinding and polishing were done, samples were put in an Isotemp Vacuum Oven 282A (Fisher Scientific) to undergo a 10 minutes baking process at 100ºC. The purpose of this process is to soften the resin so that the sample could be easily taken out of the mold.

3.1.5 Thermal etching

The polished samples were thermally etched at 1175ºC or lower temperature for 0.1 hours to provide grain boundary etching. The heating rate and cooling rate in the thermal etching process were the same as those used in the sintering process. Densities of samples were measured before and after thermal etching. The results showed that the thermal etching process did not affect the solid volume fraction obtained using Archimedes method

3.2 MICROSCOPY

To obtain necessary micrographs of those samples, the following steps were used:

(a) A Hummer 10.2 sputtering system (Anatech Ltd, Alexandria, VA) or Cressington sputter coater, 108 auto/SE (TED, Pella, Inc.) was used to coat a layer of palladium about 5 nm thick onto the etched surface to prevent charging during electron imaging by a scanning electron microscope. Coated samples were stuck onto a metal base and carbon paint was used to establish a conducting path between the metal base and the palladium layer on the samples' surface.

(b) Several images with a digital image size of 712 (width) by 484 (height) pixels were taken on randomly selected regions for each sample surface by using the secondary electron imaging mode of a Philips XL30 FEG SEM. Acceleration voltage and magnifications were chosen to best serve the requirements of analysis need to be performed (such as grain size, pore size and tessellation analysis). The other criterion for selecting magnifications is based on a

balance between the number of features in an image and the minimum measurable size (number of pixels in each feature).

i) The magnifications used for pore size, pore separation analysis and tessellation were mostly 6,250x. This magnification factor could vary depending on the solid area fraction of images.

ii) Magnifications used for grain size analysis were 50,000x.

3.3 DATA ANALYSIS

Necessary parameters needed to represent those samples were bulk density, apparent density, densification rate, pore size, pore separation, grain size, solid area fraction, and the number of pores per unit area, etc. This section describes the procedures to obtain these parameters.

3.3.1 Measurement of densities

Bulk density and apparent density were investigated using the Archimedes method. The mass of each sample was measured while the sample was dry, which was denoted as M_d. After that, the sample was placed inside a vacuum system along with a bowl of distilled water. The vacuum system was then pumped by a mechanical pump to drive air from pores of the sample. After several minutes pumping, the sample was dropped into the water bowl and stayed there for about 15 hours to allow water to flow into all the pores. After this 15 hours of soaking, the mass of the sample was measured again under two different settings. The suspended weight (denoted

as M_S) was measured while the sample was still immersed in water and an underwater supporting platform was used in the measurement. The other mass (denoted as M_i) was measured immediately after sample was taken out of water (at this time, the sample was still saturated with water). The bulk density and the apparent density were expressed below, where ρ_{theo} was the theoretical density of TZ-3YB (here the value ρ_{theo} =6.05 g/cm was used), ρ_{water} was theoretical density of water (here the value ρ_{water} =1 g/cm was used).

$$\rho_{bulk} = \frac{M_d \rho_{water}}{(M_i - M_s)\rho_{theo}} \qquad \text{Equation (3.1)}$$

$$\rho_{app} = \frac{M_d \rho_{water}}{(M_d - M_s)\rho_{theo}} \qquad \text{Equation (3.2)}$$

3.3.2 Calculation of isothermal densification rate

Plots of solid volume fraction versus log time in hours were made. The equations used to calculate densification rate during isothermal sintering and related parameters were listed below, where a was the rate constant which was obtained as a slope when we plot solid volume fraction versus log time in hours, ρ_1 was the relative density at a time of 1 hour, and ρ was the solid volume fraction at time t.

$$\frac{d\rho}{dt} = a \exp\left(\frac{\rho_1 - \rho}{a}\right) \qquad \text{Equation (3.3)}$$

Then volume strain rate was calculated as $\frac{d\rho}{\rho dt}$.

3.3.3 Measurement of average pore size, pore separation, and grain size

Average pore size, pore separation, and grain size were measured from those SEM images obtained in Section **3.2**. Parallel test lines were drawn horizontally on each image on randomly picked locations. The number of two kinds of intersection points, i.e. solid-vapor interface and solid-solid interface on lines in each image were counted. Measurements of the length of each L_v (length of each pore) were also performed. L_L (Solid length fraction) was calculated by the equation listed below and was compared with bulk density of the sample, where L was the whole length of each line and N was the number of lines on each image.

$$L_L = 1 - \frac{\sum L_v}{L \cdot N} \qquad \text{Equation (3.4)}$$

Then $V_v \approx L_L$.[40]

The number of solid-vapor interface intersection points per unit length on each line was defined as P_{Lsv} and the number of solid-solid interface intersection points per unit length was defined as P_{Lss}. Therefore, the surface area per unit volume of pore surface Sv_{SV} and grain boundary Sv_{SS} can be calculated using

$$Sv = 2P_L \qquad \text{Equation (3.5)}$$

Thus, the average pore size (average distance in the pore phase between pore boundaries) could be obtained from the following equation:[41, 42, 43, 44, 45]

$$\lambda_P = \frac{4(1 - L_L)}{Sv_{sv}} \qquad \text{Equation (3.6)}$$

Assuming all pores located on grain boundaries, equation for determining average grain intercept length (average distance in the solid phase between any types of boundary):

$$\lambda_g = \frac{4L_L}{Sv_{sv} + 2Sv_{ss}} \qquad \text{Equation (3.7)}$$

Equation for determining average pore separation (average distance in the solid between pore boundaries:

$$\lambda_{PS} = \frac{4L_l}{Sv_{sv}} \qquad \text{Equation (3.8)}$$

3.3.4 Measurement of solid area fraction and number of pores per unit area

Solid area fractions and number of pores per unit area were measured by using a digital micrographs software named ScionImage to create binary (black and white) images. Images taken of the sample using SEM were duplicated. Changes were only made in the duplicated copy. Noise was reduced by using a command "Rank Filters/ Median" as the first step. A command "Density Slice" was performed while comparing the duplicated copy with the original image before it was saved as a binary image. Some manual completion of pores was performed for each micrograph.

After software processing, pores were presented as black features while solid area was shown as white in the images. Solid area fraction was then the percentage of white pixels in the image, which can be obtained by performing "Threshold" and "Show Results" commands in the software. Solid area fraction obtained using this method could be compared with the solid volume fraction obtained from the Archimedes method in order to verify that a statistically significant number of micrographs have been used in the analysis. A 5% confidence interval was considered appropriate for the solid area fraction obtained by this software. Then the number of feature per unit area can be counted and the pore size distributions constructed.

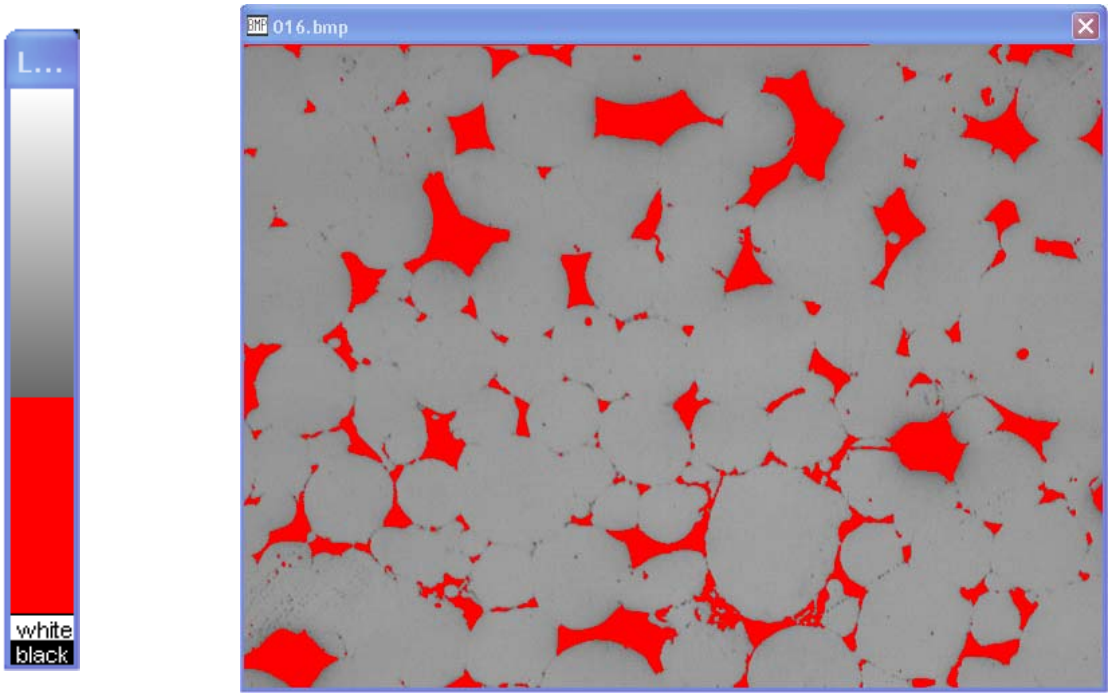

Figure 9 : Showing the density slice operation in which the top line in left toolbar is dragged to adjust the contrast of image when "Density Slice" command was performed.

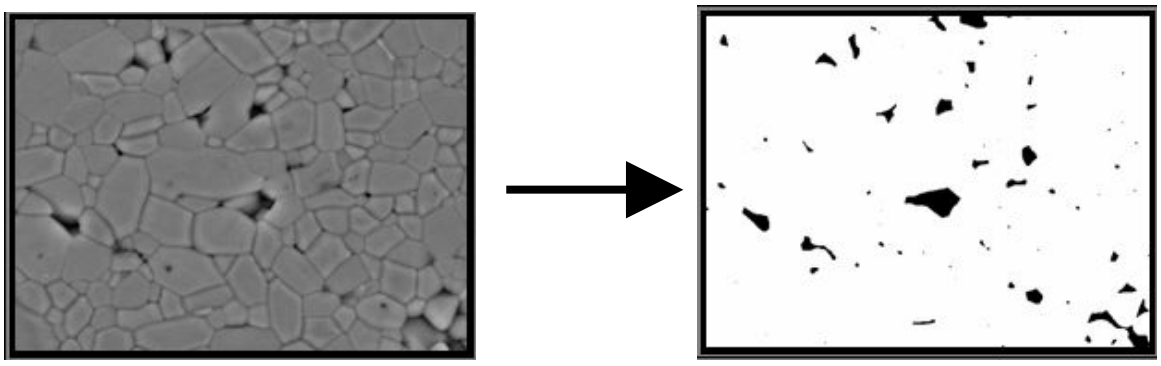

Figure 10 : The original SEM image (left) and the binary image converted from it by software "ScionImage" (right). [21]

3.3.5 Measurement of mesoscale properties

Binary images have to be obtained prior to running the Tessellator program. Any object that was smaller than 2 pixels were filtered thus very small pore features will be omitted

although we think that the number of those very small pore features is not significant. Spatial distribution of the pores was measured by a pore boundary tessellation technique . Briefly, the

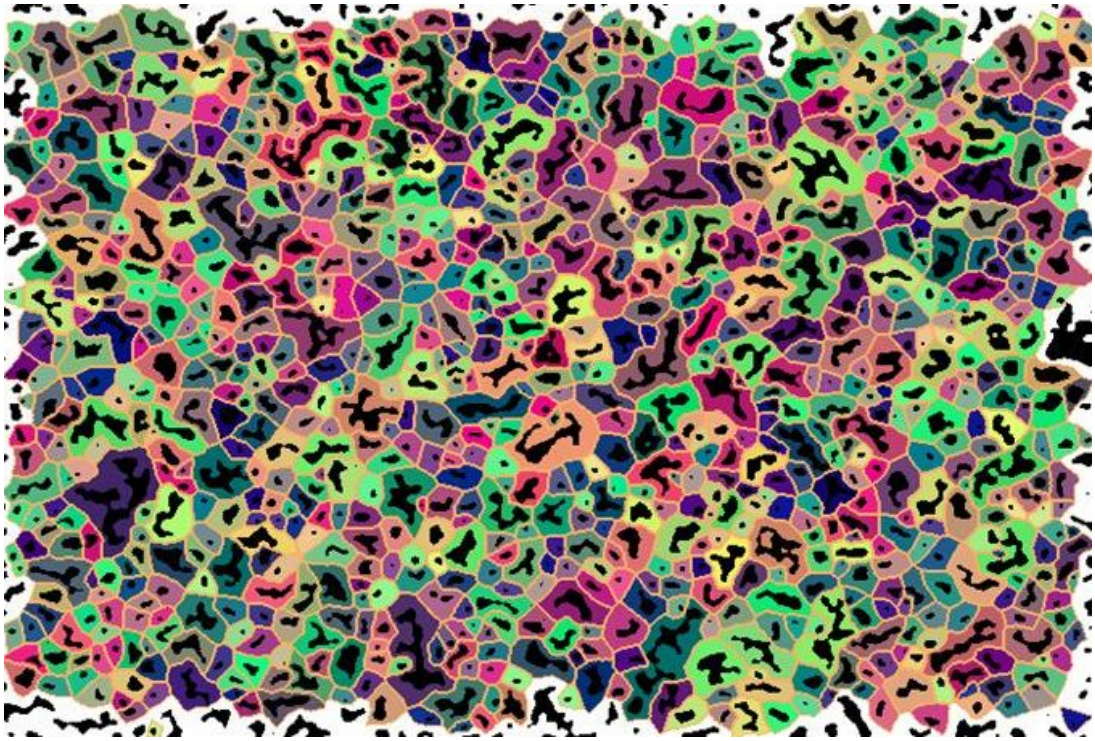

Figure 11 : A sample tessellation map. Black areas were pore areas. A cell was consisting with a pore and the area of single color surrounds the pore.

tessellation dilates the pore boundaries until they impinge on one another to create a cell structure. A pore from which the cell originated and a portion of the grains connected to the pore is contained in each tessellation cell, as showed in **Figure 12**. A tessellation cell will contain more grains due to the elimination of pore sections as the solid volume fraction of the material increases. The size of a cell by area (denoted as CA) and the pore area within the cell (denoted as PA) can be determined by running the Tessellator program. Not only have the characteristics of the pore within the cell but also the spatial arrangement and the size of the pores around the cell affect the cell properties. Therefore, mesoscale properties can be defined because the cells are larger in area than the pores and yet the area they contain is smaller than a sample area needed to

give a representative average property. One property used in this study is the local solid area fraction of the cells, SAF, which is given by:

$$SAF = 1 - (PA/CA) \qquad \text{Equation (3.9)}$$

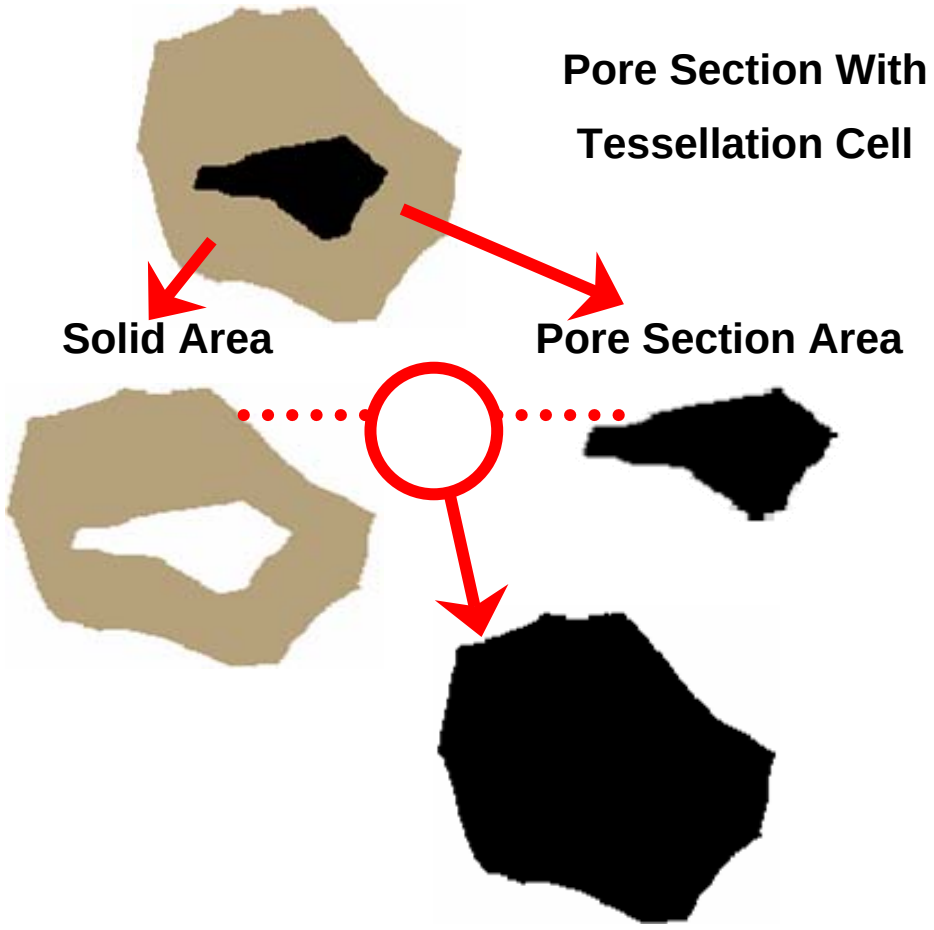

Figure 12 : Illustration of tessellation cell properties. CA, SA and PA were defined as in equation 3.9. [21]

The populations of cell properties were collected onto what are termed "cell maps" for each sintering condition. Then the evolution of the cell properties during sintering were compared and interpreted, mostly in the term of the position of the peak. A sample was showed

in **Figure 13**. Three dimensional map of **Figure 13** is shown in **Figure 14**. The height of colorful block shows the frequency of cells with corresponding CA and SAF.

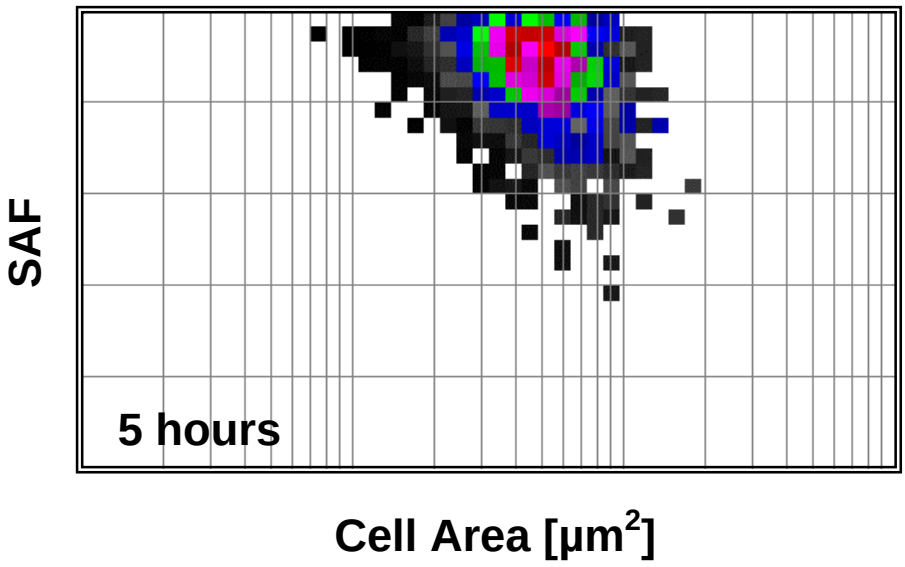

Figure 13 : A color plot of SAF-CA for a pressed ZrO_2 sample.

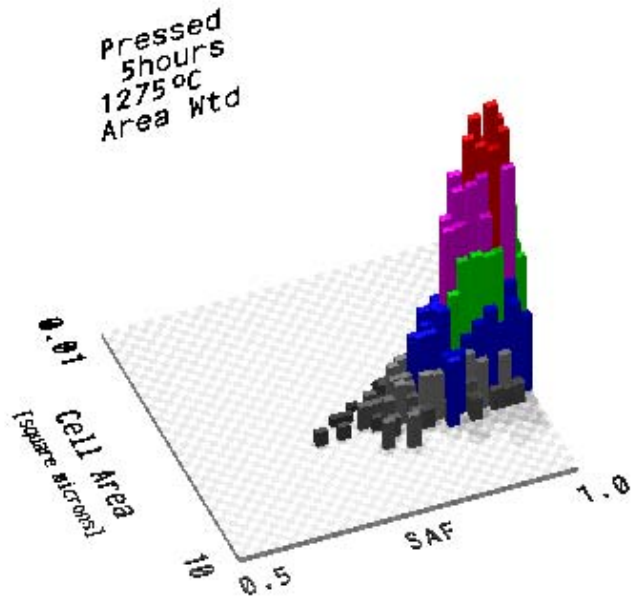

Figure 14 : A three dimensional illustration of the cell map shown in Figure 13. Height of colorful block shows the frequency of cells with corresponding CA and SAF.

4.0 RESULTS AND DISCUSSION

4.1 DENSIFICATION

Time evolution curves of the solid volume fraction (SVF) of ZrO_2-3mol%Y_2O_3 at each condition are shown in **Figure 15**. Diamonds, triangles and stars are experimental data while accompanying lines were just used as visual guides. Diamonds present samples in group LPLT, which were pressed at 51 MPa and sintered at 1275ºC for different times. Triangles present samples in group HPLT, which were pressed at 238 MPa and sintered at 1275ºC for different times. Stars present samples in group LPHT, which were pressed at 51 MPa and sintered at 1315ºC for different times.

The expected semi-log dependence behavior of SVF on sintering time, seen for many ceramics, is observed for all three sets of Zirconia samples. In other words, the sintering kinetics follows the equation shown below:

$$\rho = \rho_o + K \ln t \qquad \text{Equation (4.1)}$$

Where ρ is the SVF after isothermal sintering for a period of time t. ρ_o is the SVF after isothermal sintering for 1 hour. K is a constant. K could be viewed as the slopes of curves in a SVF-ln time graph. After fitting experimental data shown in **Figure 15** using equation (4.1), parameters ρ_o and K can be deduced. In our experiments, LPLT samples fit the equation ρ = 0.7863 + 0.0389Ln(t), HPLT samples fit ρ = 0.8703 + 0.0364Ln(t), and LPHT samples fit ρ = 0.8697 + 0.0345Ln(t). Slopes of LPLT, HPLT and LPHT were 0.0389, 0.0364 and 0.0345

[lg(hours)]$^{-1}$, respectively, which are very similar. The main difference was the density of LPLT sample was lower for a specific holding time when compared with other two sets of samples.

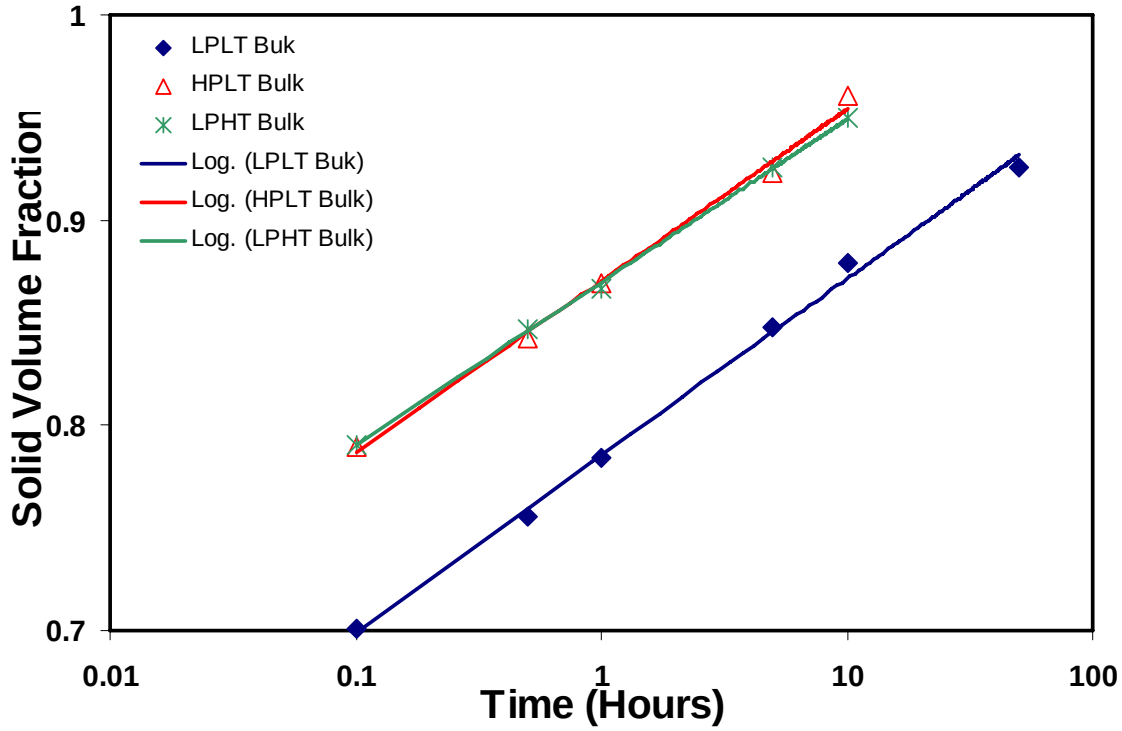

Figure 15 : The effect of sintering time on solid volume fraction of ZrO_2-3mol%Y_2O_3.

The SVF of LPLT sample is increased from 0.45 of green body to 0.70 after being heated using a rate of 5 ^{O}C/min to 1275^{O}C and held at that temperature for 0.1 hours, indicating that after this procedure approximately 50% of the pore volume in the sample was removed. An interesting result could be seen after examining the heating effects on HPLT and LPHT sets. After the same thermal treatment as the LPLT set, the SVF of HPLT samples had increased from 0.51 of green body to 0.79. For LPHT set which had the same green density as LPLT (0.45), a different isothermal sintering temperature is used. After heating to 1315 ^{O}C using a rate of 5 ^{O}C/min and holding at this isothermal sintering temperature for 0.1 hours, the SVF of LPHT sample also increased to 0.79. The SVF v.s. log time curve of LPHT samples and that of HPLT

samples are almost identical, as seen in **Figure 15**. This observation suggests that there are two ways to reach a target solid volume fraction by relatively short isothermal sintering times for this system. One way is to use a sample with higher green density to begin with. The second way is to use a lower green density sample but sinter it to a higher isothermal sintering temperature. According to the trendline equations, to obtain a full dense sample, the holding times should be 243, 35 and 44 hours for LPLT, HPLT and LPHT samples, respectively. The plot of apparent density and bulk density v.s. time is showed in **Figure 16**. At short sintering times, the apparent density is close to 100% suggesting that the pores are open. After holding 10 hours at the target temperatures, the bulk density was 0.961 and the apparent density was 0.967 for the HPLT samples, which were very close. Similarly, after same period time of holding at the target temperature, the bulk density and apparent density for the LPHT sample were 0.95 and 0.954 respectively. It suggested that the pores in these two samples were mostly isolated after 10 hours holding at the peak temperature. However, after 50 hours holding at 1275^{o}C, the bulk density and apparent density of LPLT sample were 0.923 and 0.944, a significant difference of 0.021 was calculated (as compared with a difference of 0.006 for the HPLT samples and 0.004 for the LPHT samples), which indicated that some of the pore phase in this sample were connected.

In general, the apparent density results were as expected, initially all the pores are open but at a solid volume fraction of approximately 0.9, the pores begin to close and they are all closed by the time solid volume fraction reaches approximately 0.95.

The Volume Strain Rate can be determined by differentiating the experimentally fitted equations shown in **Figure 15**. The plot of volume strain rate [$d\rho/(\rho dt)$] v.s. Solid Volume Fraction is shown in **Figure 17**. As exhibited in this graph, densification rates for all samples do not reach a zero value after the longest sintering time used in our experiments, suggesting that all

sintering processes were not exhausted. Again, the curve of LPHT samples and that of HPLT samples are almost identical which is not surprising since same sets of data is used for **Figure 15** and **Figure 17**. All three curves in **Figure 17** have similar shapes, suggesting that they are governed by a same rule. **Figure 17** agrees with the general trend for isothermal sintering in

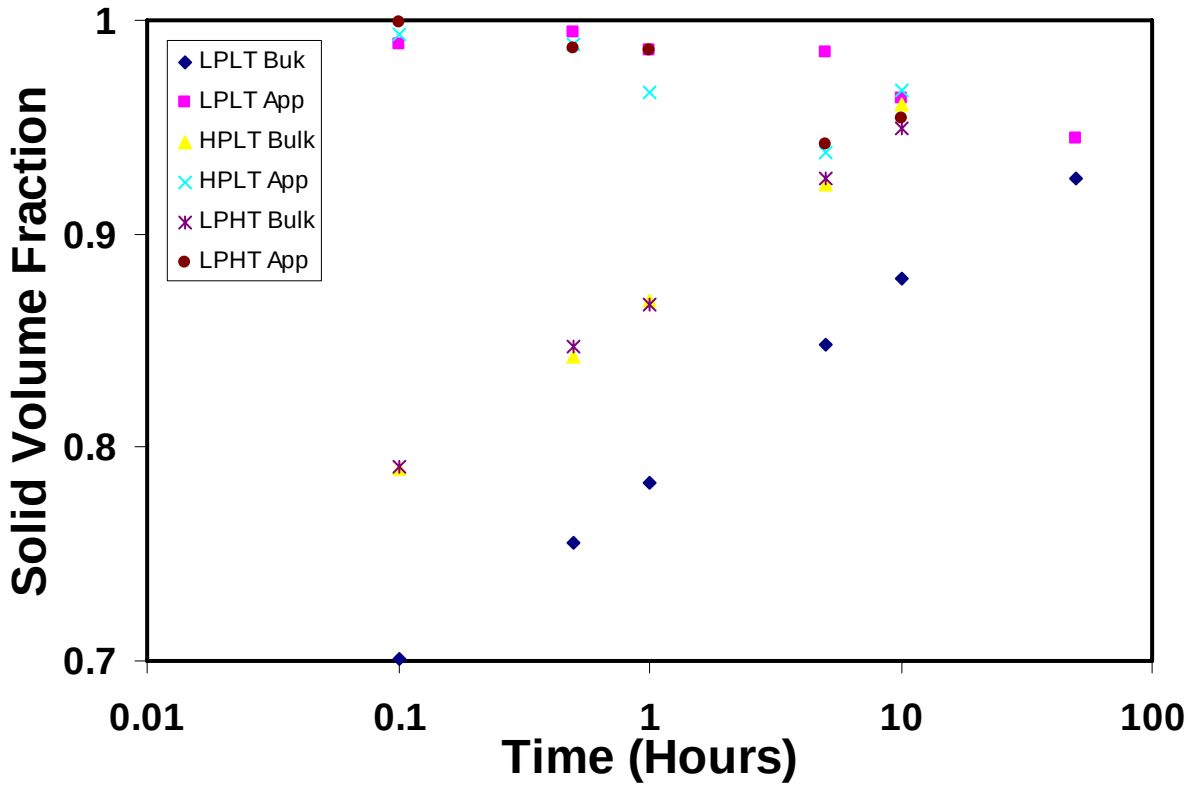

Figure 16 : Comparison of Apparent Densities and Bulk Densities of the Zirconia samples studied here.

which volume strain rate decreases with increasing isothermal sintering time. However, we notice that for the same value of solid volume fraction, values of volume strain rate of samples in group LPHT and HPLT were larger than those of samples in group LPLT. E.g., when the solid volume fraction of samples of group LPHT and HPLT both had a value of 0.79, the volume strain rates were 0.44 and 0.42 respectively. In contrast, the volume strain rate was only 0.053 for the sample having a solid volume fraction of 0.78 in group LPLT. It indicates that when they

have same solid volume fractions, LPHT and HPLT samples have higher densification rates than LPLT samples, which probably due to the fact that they reached higher densification rates during heating to the sintering temperature, although this can not be confirmed by these isothermal experiments.

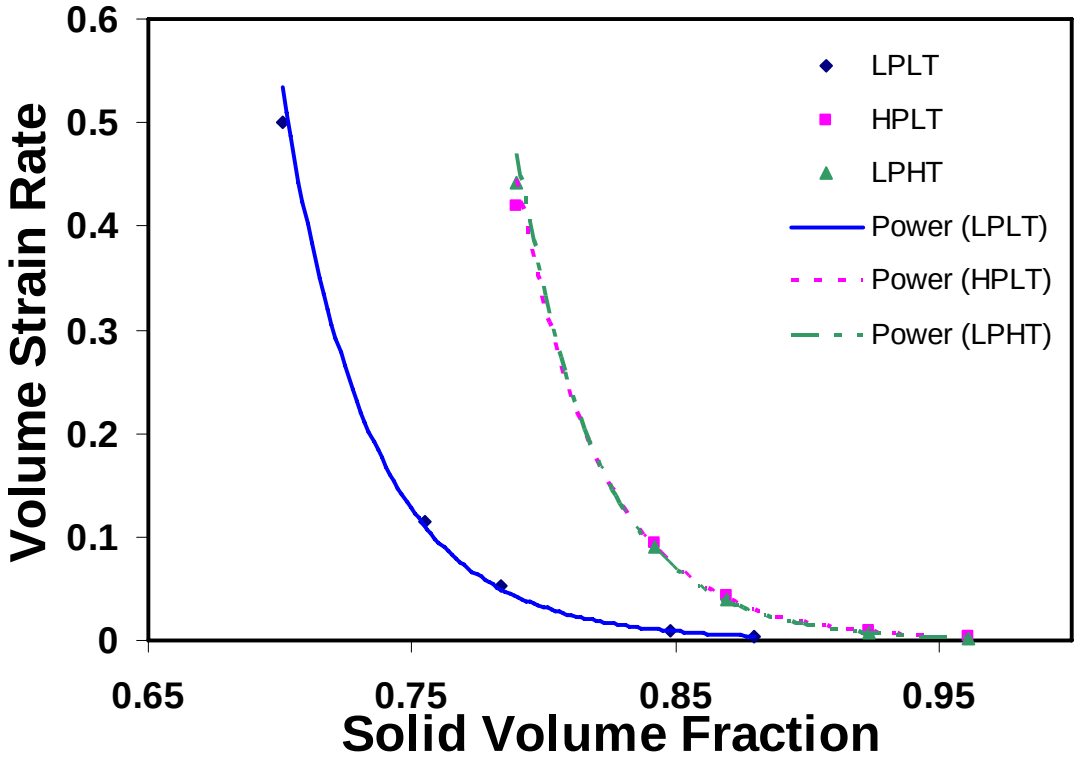

Figure 17 : The relationship for isothermal sintering of LPLT, HPLT and LPHT between volume strain rate and solid volume fraction.

Densification in ceramic materials is assumed to be dominated by uniform neck growth between particles by mechanism such as grain boundary or volume diffusion. (See **Figure 18**.) Two factors play a role in neck growth. One is the contact area between particles; the other is the velocity of flux through the contacting areas. Since the green body processing was the same for samples in LPLT and LPHT groups, the same green body densities resulted for both sample sets. However, 1315^{O}C was used as holding temperature for LPHT samples, which is 40^{O}C higher

than the holding temperature used for LPLT samples. It is reasonable to suggest that LPHT samples reached a higher densification rate during heating since higher temperatures provided higher diffusion rates. This is required for faster neck growth and hence densification.

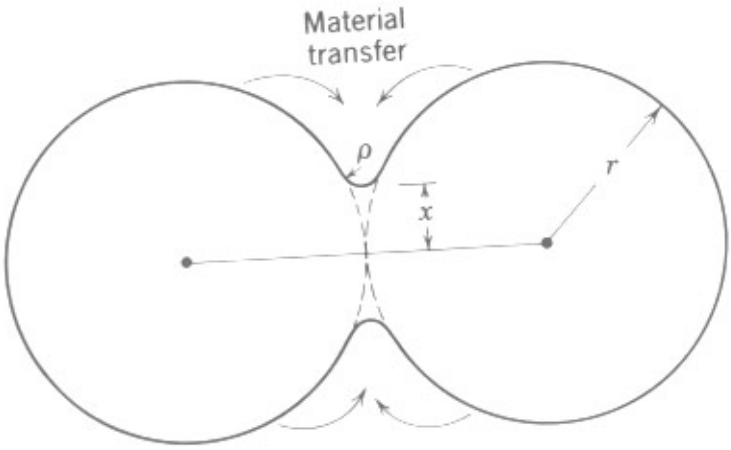

Figure 18 : Illustration of uniform neck growth between two ceramics particles by mechanism such as grain boundary or volume diffusion.

A pressure of 238 MPa was used to press green bodies of HPLT samples, which is much higher than the pressure of 51 MPa used for LPLT samples, although they were sintered using same heating rate and same holding temperature afterwards. Higher pressure used in the HPLT samples fabrication leads to higher green density, fewer large pores and more contacts between particles. As a result, more necks form between particles which is thought to have accelerated densification associated with neck growth in HPLT sample. All these materials have green densities well below packing density associated with dense random packing (0.66). Therefore particle rearrangement is necessary in order to achieve full density. The need to rearrange will slow down formation of new necks and lower densification rate and this may explain the effect of green density on densification.

4.2 AVERAGE GRAIN INTERCEPT, PORE SIZE AND PORE SEPARATION

The effect of green density on sintering behavior has been reported previously. [36, 46] In general, the effect is thought to be that the wide pore size distribution associated with low green density affect coarsening of the grain structure (wider distributions tend to drive coarsening or ripening processes) and coarsening increases the separation of sinks for diffusion and decreases densification rate. Thus, it was necessary to obtain certain microstructure results such as average grain size, pore size and pore separation in this study in order to determine if the observed effect of green density on densification rate is associated with coarsening. Previous studies have shown that this system (ZrO_2-3mol%Y_2O_3) goes through densification by grain boundary diffusion[47] and a severe $1/\lambda g^4$ dependence of densification rate is thus expected. [30] Therefore coarsening of the grain structure could have a dramatic effect on densification rate.

Average grain intercept length, average pore intercept length and average pore separation intercept length (as defined in Section **3.3.3**) were measured from SEM images, characterizing the average size of the grains, pores and the average separation between adjacent pores respectively. The measured dependence of these three size parameters on solid volume fraction was shown in **Figure 19** and **Figure 20**. All error bars in this study is calculated as the 95% CI between the images. Equation (4.2) is used to obtain the value of error bar, where σ is the standard deviation for a pool of values obtained from individual images and N is the number of images that being analyzed.

$$95\%CI = \frac{2 \cdot \sigma}{\sqrt{N}} \qquad \text{Equation (4.2)}$$

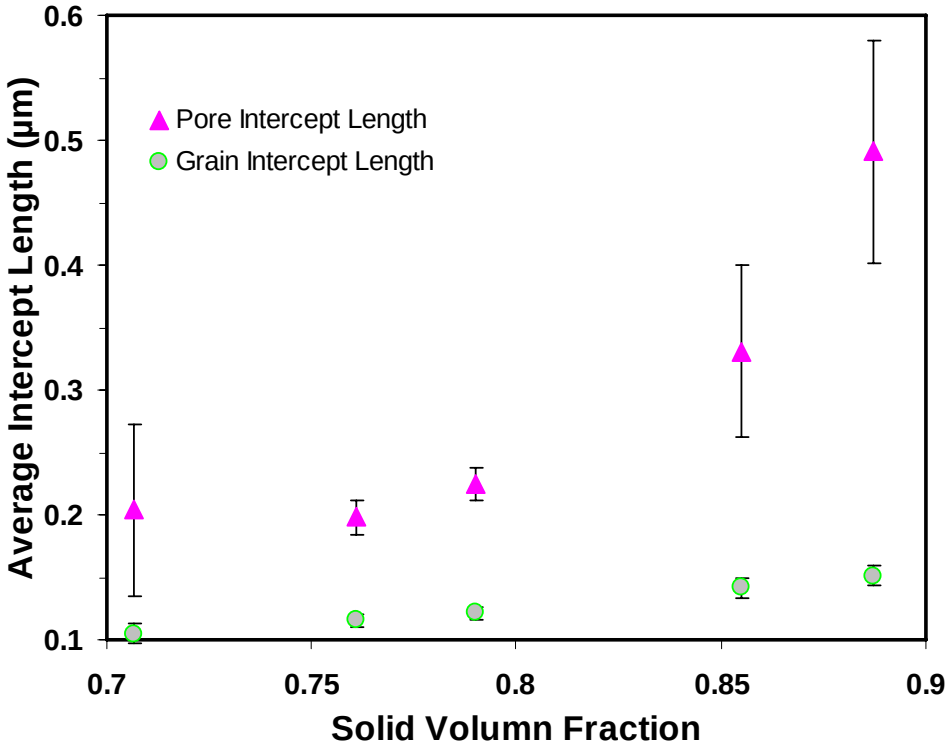

Figure 19 : The average grain intercept lengths and pore intercept length plotted against solid volume fraction for LPLT samples.

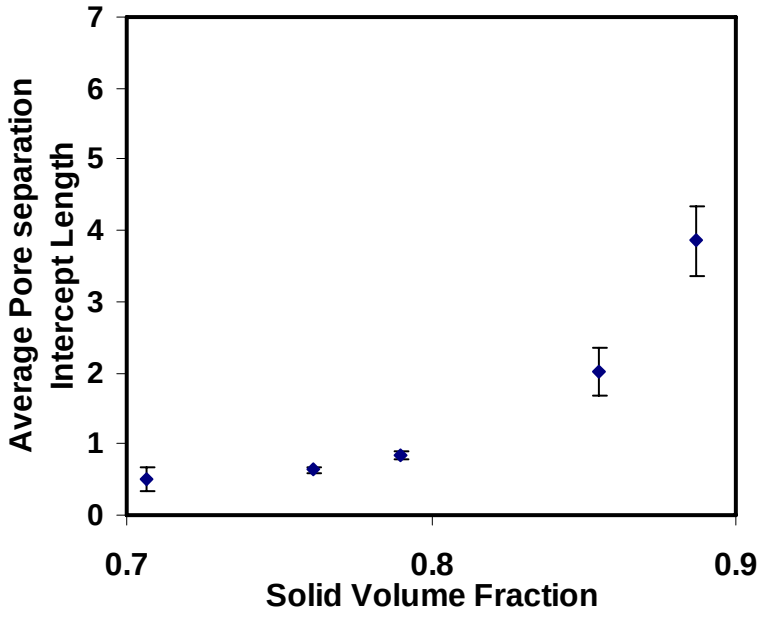

Figure 20 : The average pore separation lengths of LPLT samples plotted against solid volume fraction for LPLT samples.

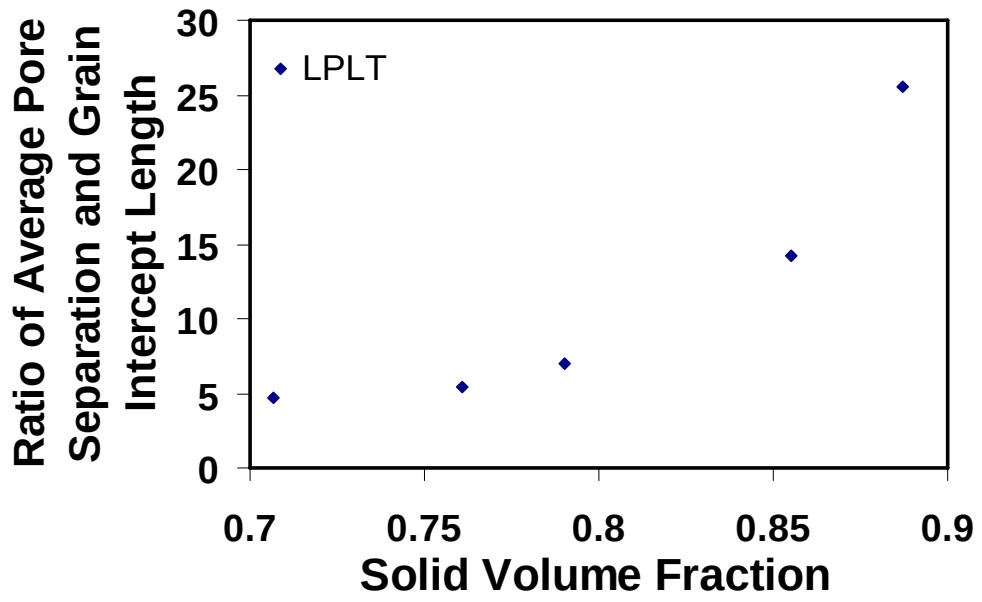

Figure 21 : Plot of ratio of average pore separation intercept length and grain intercept length against solid volume fraction.

As shown in **Figure 19**, the average grain intercept length of LPLT is 0.1 μm at a solid volume fraction of 0.71 and then increases slowly to 0.15 μm at a solid volume fraction value of 0.88 after 10 hours sintering. The slowly increase agrees with previous results in literature[48] that suggests grain growth is very slow in this system. Also, over the same range of solid volume fraction the average pore intercept length increased from 0.20 to 0.49μm. The increase of average intercept length of pores is greater than that of grains. In contrast, we observed a considerable increase in the pore separation. The pore separation increased from 0.49 μm to 3.85 μm over the same range of solid volume fraction mentioned above. As seen in **Figure 21**, the ratio of pore separation (3.85 μm) to average grain intercept length (0.15 μm) was more than 25 at a solid volume fraction value of 0.89, which was much greater than the value of 4.7 when the solid volume fraction was 0.71. A previous study showed that commercial alumina powder with a bulk green density of 0.57 (much higher than samples in this study) after dry pressing has a

much lower ratio during sintering than these LPLT samples studied here. After 10 hours sintering, that alumina has a pore separation to grain intercept ratio of less than 5 at a solid volume fraction of 0.89.[46] This previous study with commercial alumina powder showed that the number of pores per unit area did not decrease much below a solid volume fraction of 0.9 and agrees with the common expectation that pore elimination does not begin to affect the results until pores pinch off and become isolated in final stage of sintering. The commonly accepted correlation between the diffusion length for the dominant mass transport mechanism and grain

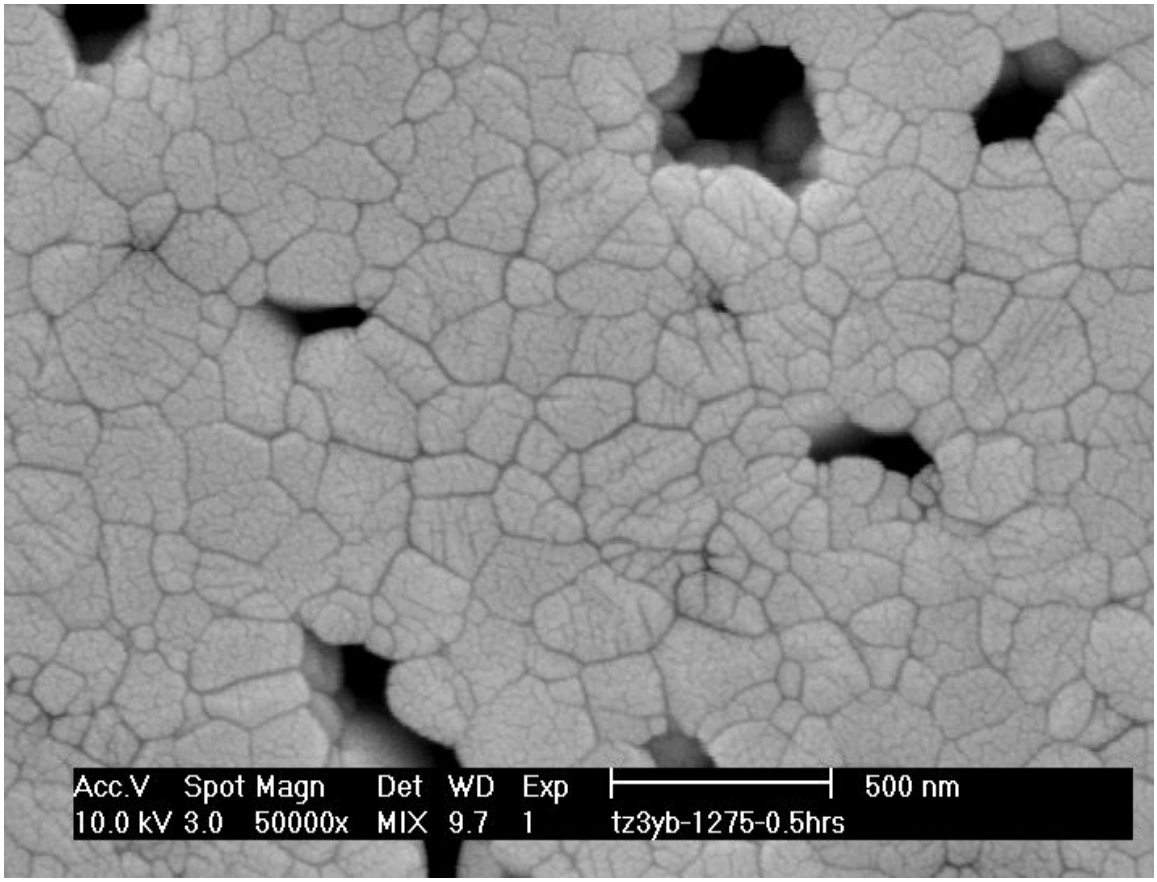

Figure 22 : A high magnification SEM image shows there is few pores in triple point on polished cross-section of this zirconia ceramics.

size are based on the sintering models that assume pores exist on all grain edges during intermediate stage of sintering or on all grain corners or triple points (points between three

adjacent grains) during final sintering stage. If this assumption was correct, there would be no difference in the ratio of grain intercept to pore separation between alumina and zirconia ceramics. This assumption might not be true in our case, since the average separation of pores we observed is much larger than the grain size. In addition, as shown in Figure 22, pores were not observed in triple-point in this zirconia material when the imaging resolution is about 7 nanometers.

It is important to know if our measured results are representative and not systematically biased by not detecting very fine pores. For samples in the group LPLT, L_L from the image analysis are about the same with the solid volume fraction measured from the Archimedes method, which means the SEM images taken in limited locations can well represent the whole sectioned surface statistically. The Solid Area Fractions of those SEM images measured by the software Scion were 0.78, 0.82, 0.87 and 0.93 for 0.5 hours, 1 hour, 5 hours and 10 hours respectively, which were close to but slightly higher than Vv measured by Archimedes method of 0.76, 0.79, 0.86 and 0.89. This suggests no statistically relevant population of small pores was missed. It is of course possible that a few small pores were missed but they were not statistically significant. In summary, the above discussions suggest that for our zirconia samples grain intercept length did not relate to diffusion length in the way as assumed by the models and all the interpretation of experimental results associated with them. This is because the pore separation is much larger than the grain size at any particular solid volume fraction and increases faster with sintering. Instead, pore separation measured in this material could correlate more strongly with diffusion length than the grain size and suggests that pore separation is a better representation of the microstructrual scale in sintering contrary to the assumption of microstructure maps are based on traditional sintering models and only use grain size.[49, 24] This may not be general to all

ceramics because of very slow grain growth in this system. **Figure 23** shows a new concept model that does not require pore channels on every grain edge (triple point) during sintering. All of the sintering models require uniformly distributed vacancy annihilation along grain boundaries with pores separated by only one grain boundary. **Figure 23** illustrates how the proposed mechanism involves diffusion creep to allow uniform distribution of vacancy annihilation along the grain boundaries with more than one grain in the unit cell. In **Figure 23**,

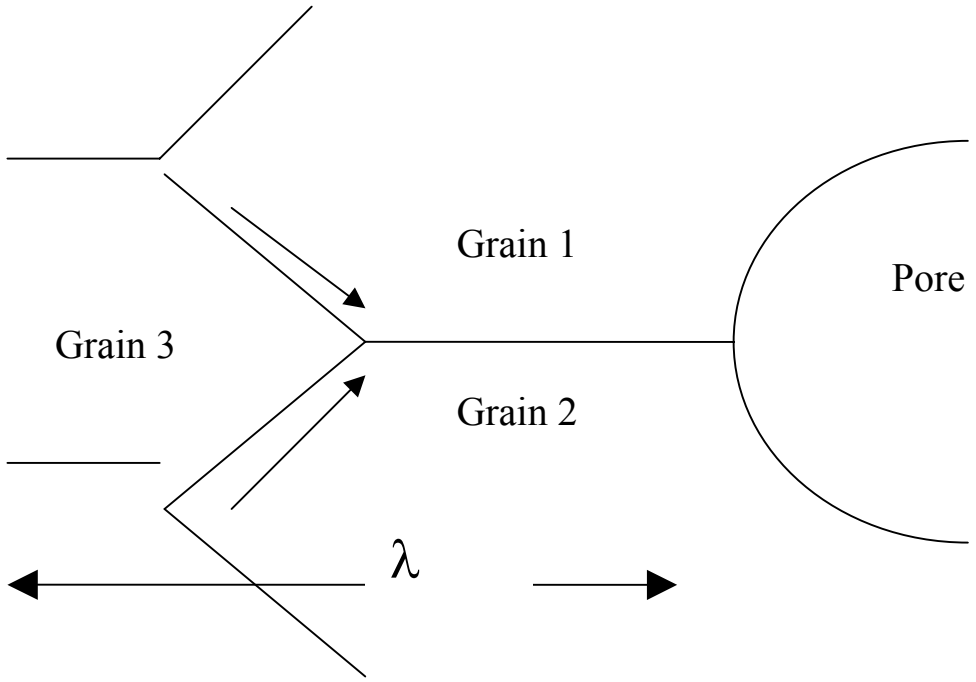

Figure 23 : A two dimensional representation of a microstructure with more than one grain between pores. Vacancy annihilation on boundary between grain 1 and grain 2 would create tension without mass transport along boundaries between grain 1 and grain 3 and boundaries between grain 2 and grain 3 in response to stress.

the vacancy annihilation along grain boundary between Grain 1 and Grain 2 would create tension on boundaries between Grain 1 and Grain 3 and between Grain 2 and Grain 3. This would drive vacancy diffusion along these boundaries and consequent vacancy annihilation. Therefore it is possible to have more than one grain in a unit cell as long as there is uniform annihilation of vacancies along all grain boundaries. Thus grain boundary diffusion would control the necessary

creep and densification. However, the diffusion length most correlates with the average pore separation is not the grain size. This conceptual model would lead to the conclusion that coarsening, as reflected in the pore separation length, is occurring much more quickly than one would suspect from the grain size plotted in **Figure 19**. This is therefore responsible for the decrease in densification rate. It is now necessary to determine the cause of the observed increasing in pore separation and pore coarsening. This can be done using the pore size distribution.

4.3 PORE SIZE AND DISTRIBUTION FOR LPLT SAMPLES

After examining the images of polished sections of samples in group LPLT, pore size distribution (in two dimensions) were determined. **Figure 24** shows the number of pores per unit

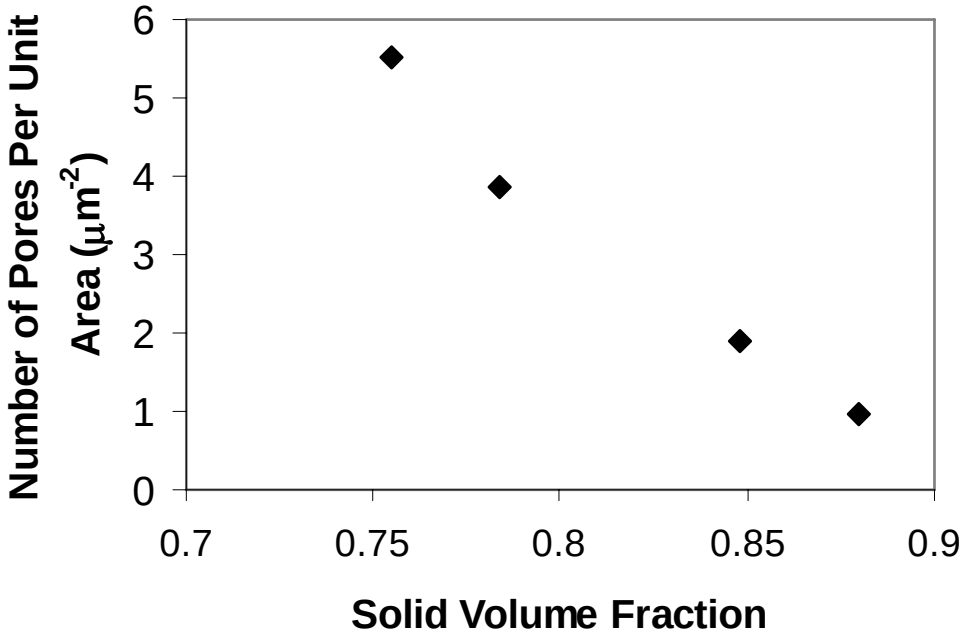

Figure 24 : The number of pores per unit area plotted against solid volume fraction for LPLT samples.

area for samples for the different solid volume fractions. The number of pores per unit area decreased smoothly from 5.53/μm^2 to a value of 0.96/μm^2 when solid volume fraction increased from 0.76 to 0.89. This result suggests that unlike in the sintering models in which neck growth causes uniform shrinkage of pores but not pore elimination, densification in this system involves a lot of pore elimination. Plots of Frequencies of Pores by Area v.s. Pore Section Area in **Figure 25** also indicates that pore elimination plays a larger role in densification compared to pore shrinkage during the isothermal sintering process. As seen in **Figure 25**, for the 0.5 hours

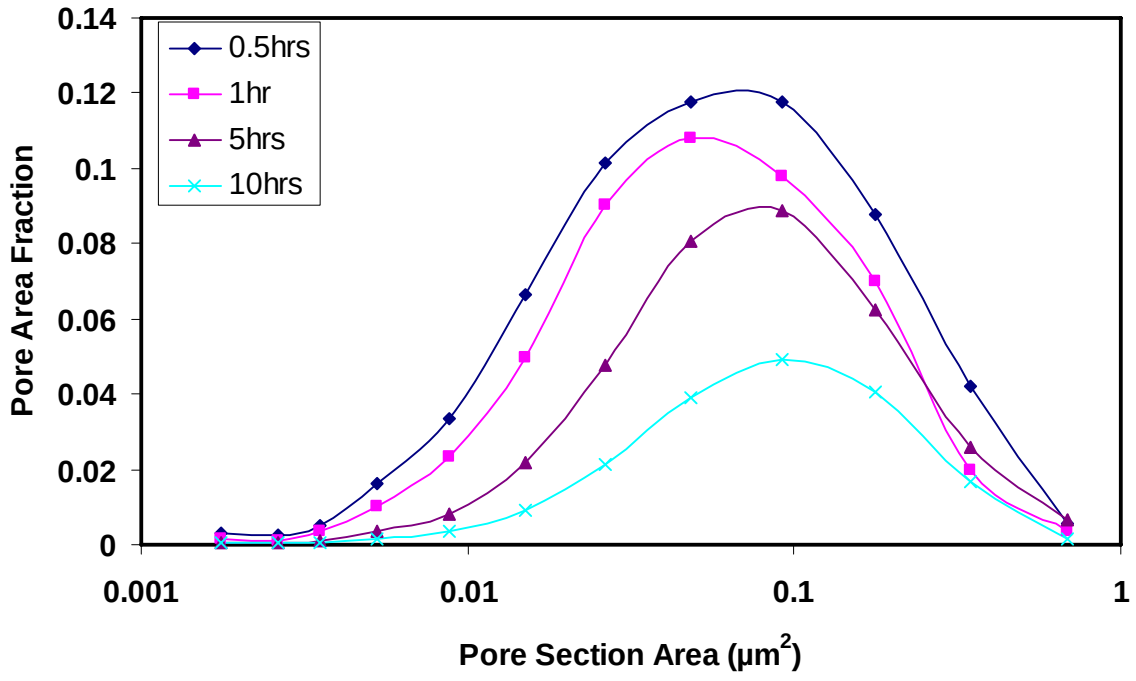

Figure 25 : The effect of sintering time on the pore area distribution by area for samples with a green density of 0.45 sintered at 1275^{O}C.

sample, at a solid volume fraction of 0.76 the distribution of pore section areas extends from 0.002μm^2 to 1 μm^2 with an average of 0.05 μm^2. By using the equation $A=0.25\pi d^2$, the average corresponds to an equivalent circular diameter is 0.25μm, which is greater than the grain size (0.16μm) calculated from the average grain intercept, emphasizing the pores are larger relative

compared to the grain. As shown in **Figure 26**, as isothermal sintering progresses, the average pore area increases, which evidences that pores with area below the average at the beginning of the sintering appear to be eliminated somewhat faster than those above the average size. This suggests that the elimination of small pores was more significant than shrinkage of large pores.

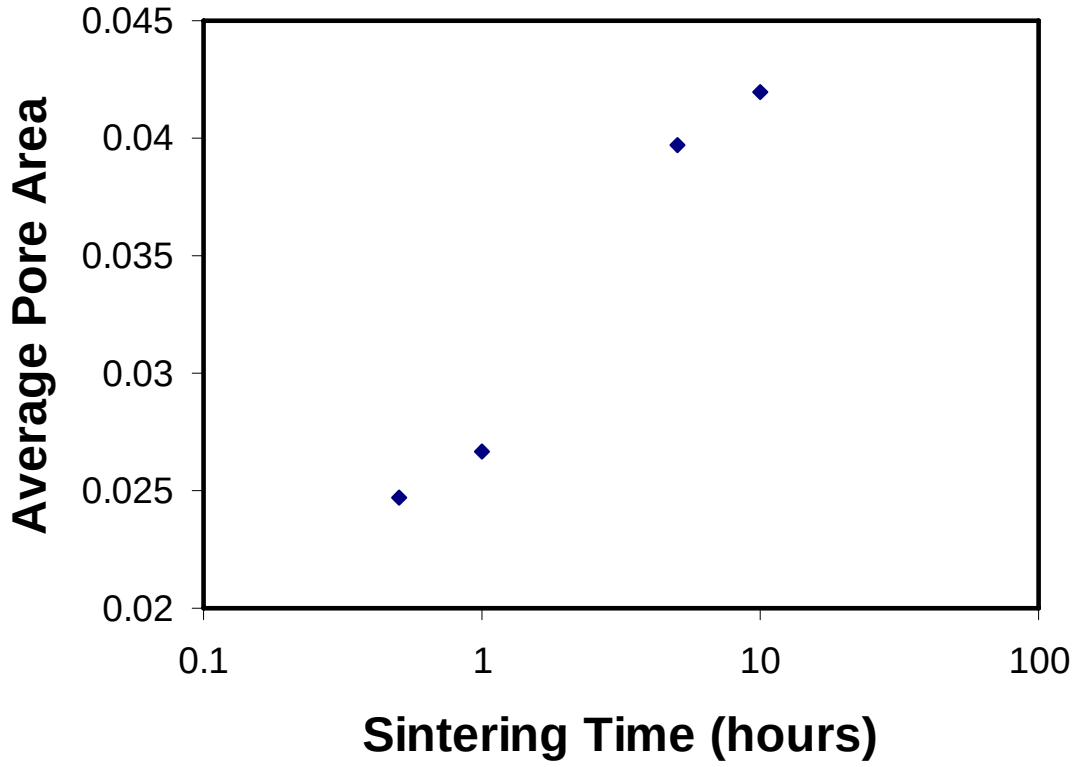

Figure 26 : The plot of average pore area against sintering time for LPLT samples.

4.4 TESSELLATOR RESULT OF LPLT SAMPLES

The mesoscale structure of LPLT samples was determined by using software called Tessellator. (Defined in section **3.3.4**.)

Figure 27 and **Figure 28** showed frequencies of Cell Area (CA, defined in section **3.3.4**) and Local Solid Area Fraction (SAF, defined in section **3.3.4**) of cells in the tessellation map of a LPLT sample which was held at 1275^{o}C for 5 hours to give a solid volume fraction of 0.85. If these two plots are combined, a "cell map" of the solid area fraction (SAF) of the cell against cell area (CA) was obtained. **Figure 29** shows a cell map of the solid area fraction of the cell against cell area, the different colors represent arbitrarily chosen ranges of relative frequency and they are solely used to help readers observe the details of the distribution. A three dimensional demonstration of this plot was shown in **Figure 30**. The information derived from the tessellation is two dimensional and cannot be interpreted in three dimensions without assumptions. In this respect it is no different from any population measurements taken from image analysis of planar surfaces including particle size distributions. Nonetheless meaningful interpretations can be made.

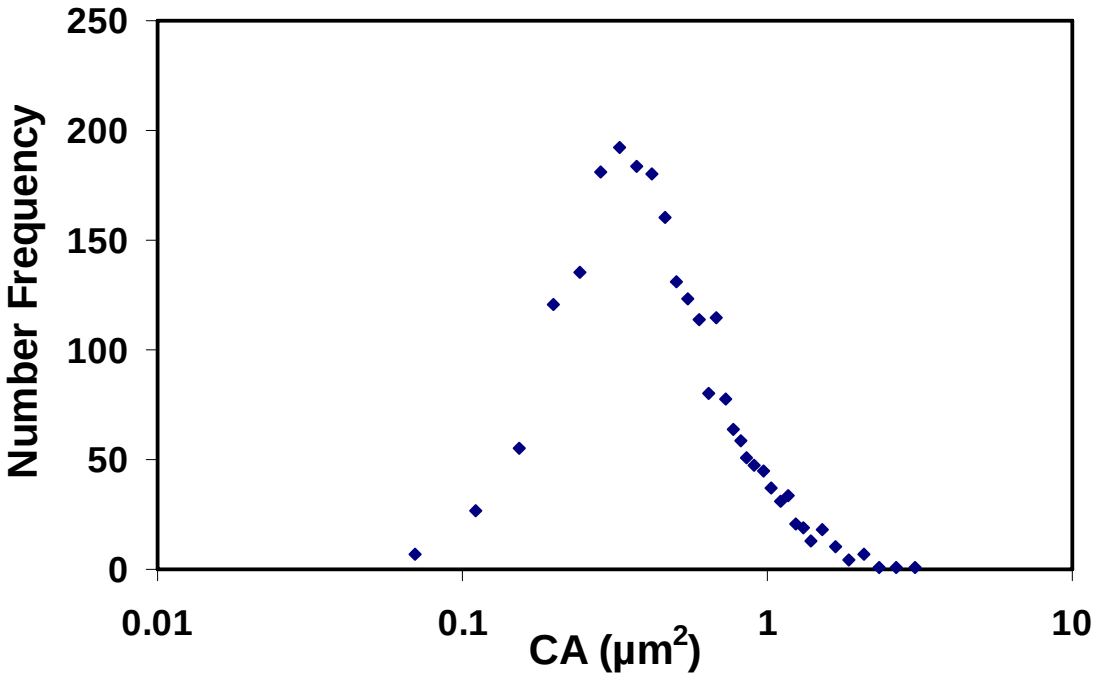

Figure 27 : Frequencies of cell area for cells on a tessellation map of the sample which was held at 1275^{o}C for 5 hours in group LPLT.

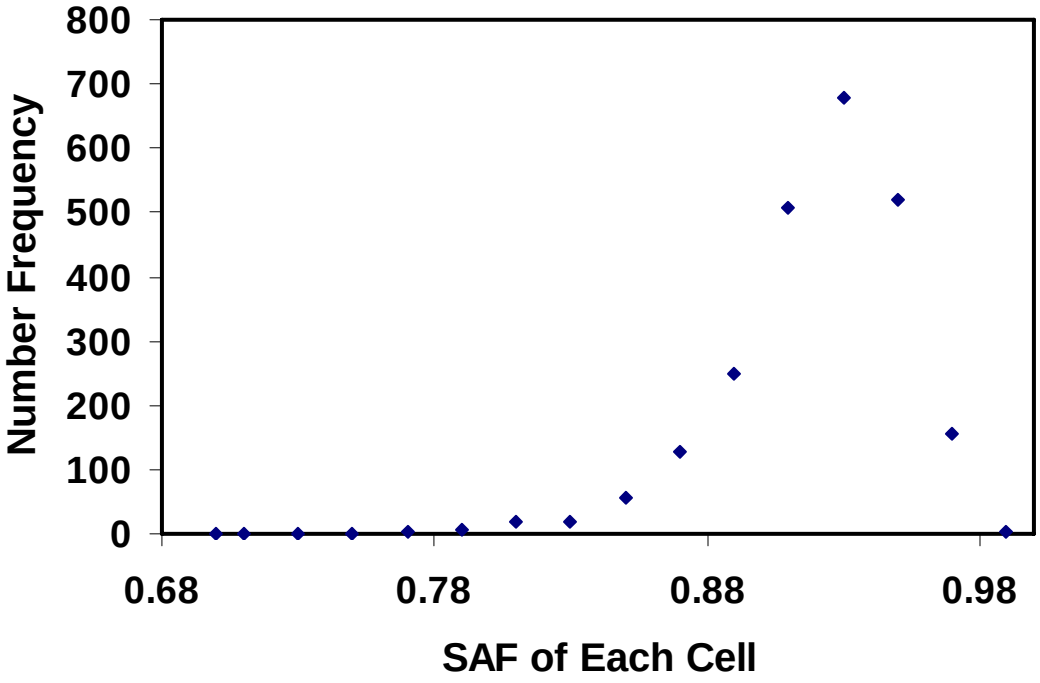

Figure 28 : Frequencies of solid area fraction (SAF) for cells on a tessellation map of the sample which was held at 1275°C for 5 hours in group LPLT.

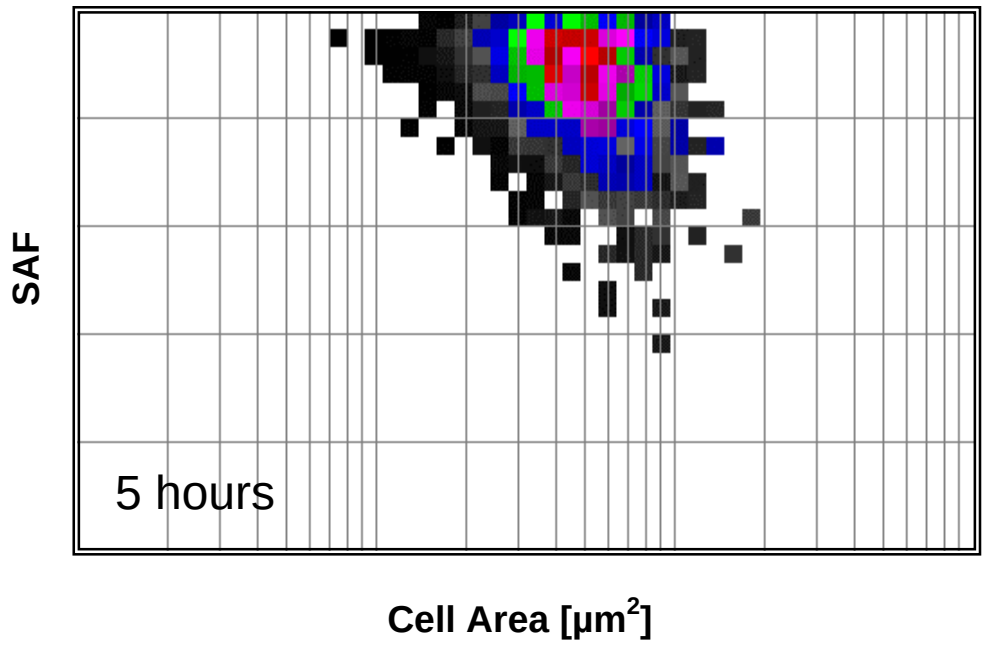

Figure 29 : The plot of tessellation cell solid area fraction (SAF) against cell area (CA) for LPLT sample fired for 5 hours. The different colors represent ranges of relative frequency and are used to help show the shape of the distributions. Note that CA is plotted on a logarithmic scale.

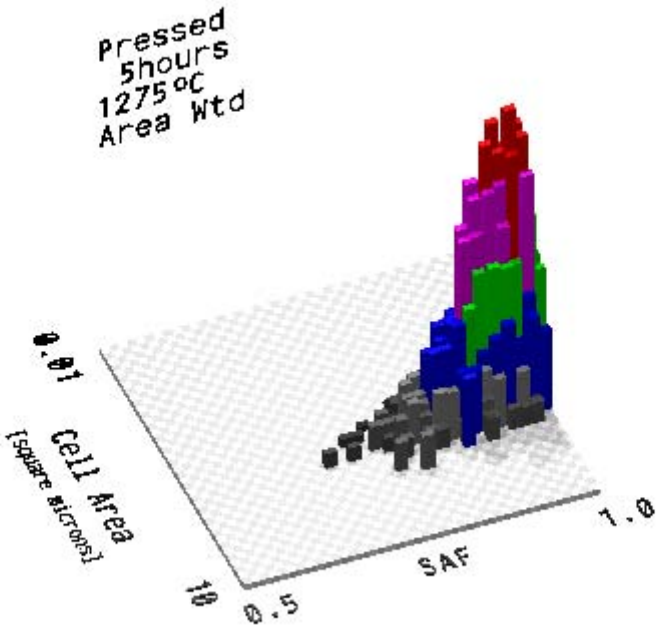

Figure 30 : A three dimensional demonstration of the cell map.

The trends in the evolution of the cell maps during sintering can be interpreted in terms of the position of the intervals in the highest frequency range, which will be termed the "peak". As shown in **Figure 31**, after 0.5 hours at 1275 ^{O}C, the solid volume fraction is 0.76 and the population on the cell map is relatively broad. The solid area fraction of the cells has values as low as 0.65. The peak is broad, extending along a line from SAF = 0.82 and CA = 0.35 μm^2 to SAF = 0.97 and CA = 0.15 μm^2 while centering at approximately SAF = 0.9, CA = 0.2 μm^2. It is worth noting that the peak position is at much higher values of SAF than the solid volume fraction of the sample (0.855) and that observed for the commercial alumina pressed to a green density of 57 % and fired to roughly the same solid volume fraction.[50] The peak for alumina occurred at SAF = 0.7 at a solid volume fraction of 0.78. It can be concluded that the zirconia in

our study, shows evidence of the formation of relatively large, dense regions at lower solid volume fractions when compared to the commercial alumina. This could be associated with the pore elimination observed in the pore distribution results, which is thought to be caused by spatial heterogeneity in the green microstructure of the zirconia resulting from the less efficient packing of particles and a reduction in the green density.

The results of current study are also consistent with previous densification simulations of sintering by contact flattening in that neck growth would be more advanced in regions of highly coordinated particles in heterogeneous green compacts.[51] This would lead to elimination of fine pores in these regions and would result in tessellation cells of higher SAF.

When the sintering time increases, the population in SAF-CA space became narrower, as evident in **Figure 31**. Therefore the microstructure is evoluting towards higher spatial homogeneity at the scale of the tessellation cells. There is also a significant shift in the peak of

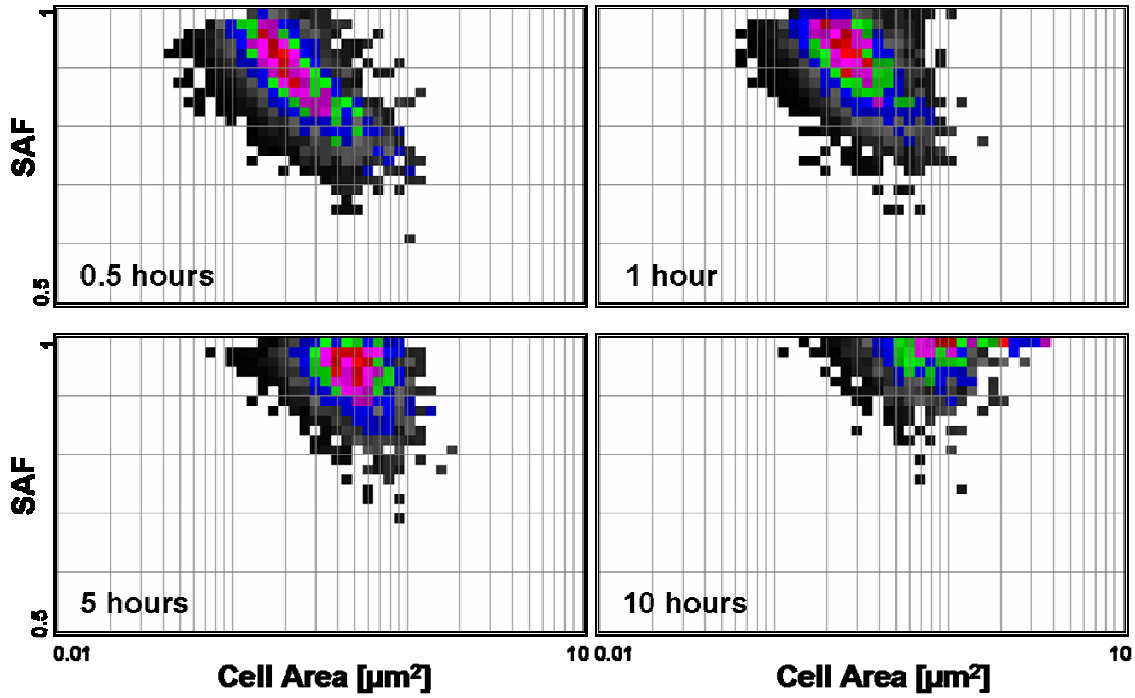

Figure 31 : Plots of tessellation cell solid area fraction (SAF) against cell area (CA) for samples fired for 0.5 hours, 1 hour, 5 hours and 10 hours. The different colors represent ranges of relative frequency and are used to help show the shape of the distributions. Note that CA is plotted on a logarithmic scale.

the SAF-CA population. After 5 hours the solid volume fraction of the material has increased to 0.87 and the peak had moved to higher values of SAF and CA to be centered at SAF = 0.95, CA = 0.5 μm^2. Finally after 10 hours the peak is at SAF = 0.98, CA = 0.85 μm^2. Such an increase in SAF and CA during sintering has been previously interpreted as pore shrinkage and elimination, similar to that commonly expected in final stage sintering.

In summary, the results of this set of pore distribution measurements on LPLT gives a clear picture of the microstructural evolution for a zirconia ceramic sintered from a low green density. While the effect of isothermal sintering time on the sintered density was not surprising, the pore separation measurements suggest that the microstructure was coarsening much faster than one would expect by considering the evolution of the grain size. Therefore, the often assumed association of the diffusion length with the grain size must be reconsidered in this case. The coarsening of the structure, as reflected in the evolution of the pore separation, is not thought to result from the effect of a different mass transport process such as surface diffusion that coarsens the grains in porous ceramics. Instead, a coarsening results from pore elimination by densification along a microstructural pathway that is caused, in part, by the low green density and inhomogeneous green microstructure. This interpretation assumes that the low green density is a consequence of inhomogeneous packing of particles in the compact. In this circumstance, regions of highly coordinated particles sinter by neck growth to produce relatively dense areas early in sintering. Obviously this must occur without significant differential sintering of these regions relative to their surroundings. The pore boundary tessellation detected the formation of these relatively dense regions at solid volume fractions of 0.76, well before there are any major effects on the ratio of pore separation to grain size, as seen in **Figure 32**, the difference of the ratio of pore separation to grain intercept between the previous studied commercial alumina and

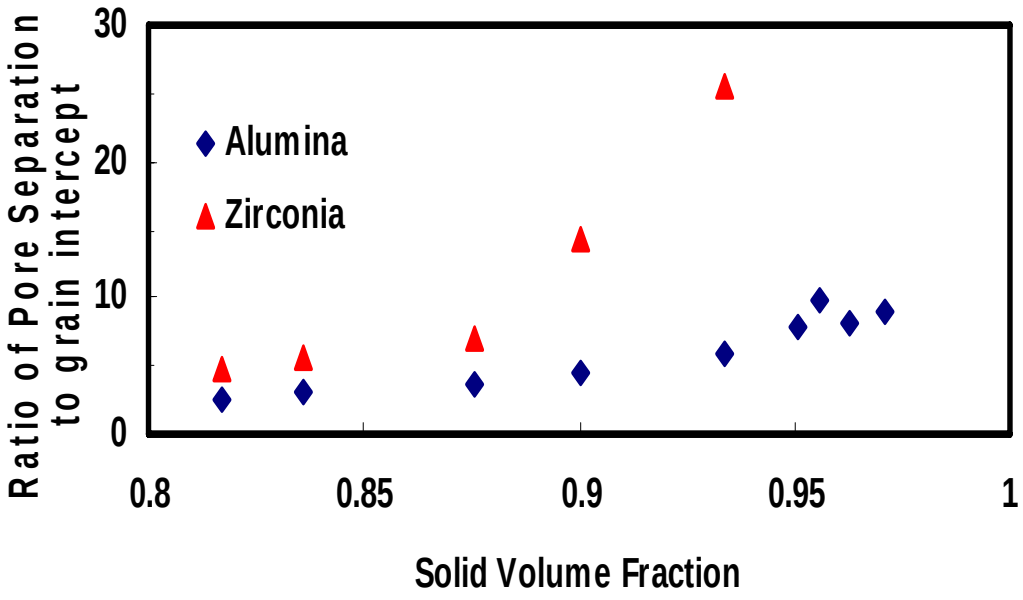

Figure 32 : Comparison of ratio of pore separation to grain intercept length between previous studied commercial alumina and the zirconia materials in this study.

the zirconia materials in this study became noticeable when sample's solid volume fraction exceeded 0.85. The dense regions of zirconia materials can be clearly seen in the microstructure of material sintered at 1275 ^{O}C for 1 hour in **Figure 33**. Roughly five grains can be counted along the diameter of dense areas in this image. Continued densification and pore elimination causes the dense area to grow. The elimination of relatively small pore sections causes the average pore section area to increase. **Figure 34** shows the numerous small grains between widely spaced pores in material sintered for 5 hours. The evolution in the SAF-CA maps shows that the material becomes more spatially homogeneous as sintering continues. However, the ratio of the pore separation to grain size increases to 20 after 10 hours of sintering. Given the functional dependence of densification rate on the scale of the microstructure, coarsening by pore elimination will have a profound effect on the predicted rate of densification during intermediate stage sintering and throughout final stage sintering. The implications of this for the sintering of

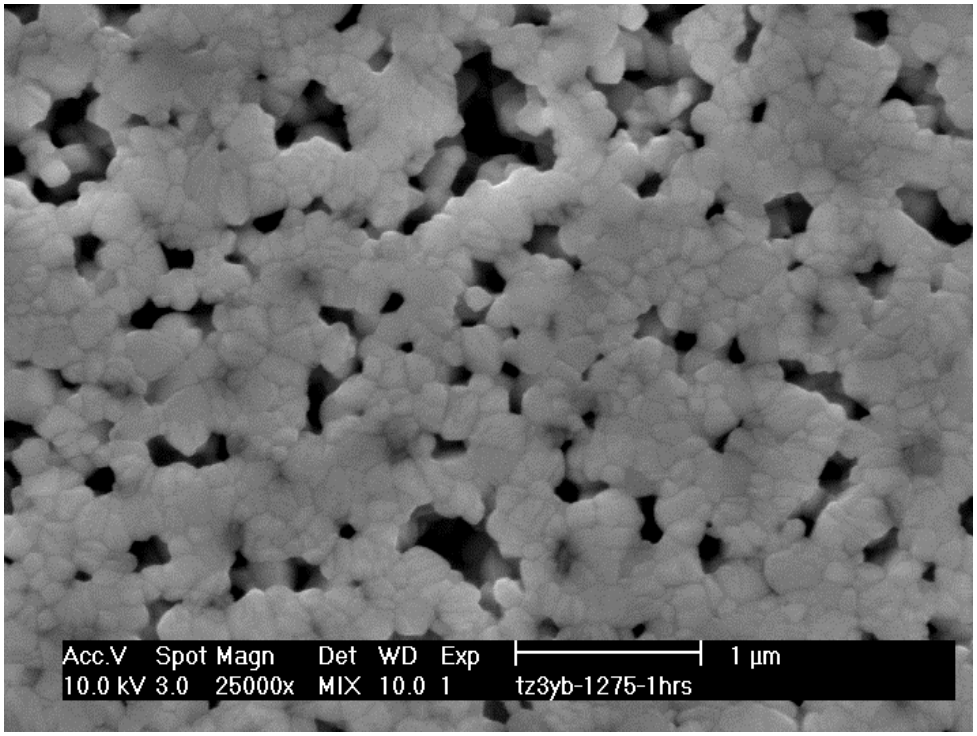

Figure 33 : The microstructure of a sample sintered for 1 hour at 1275^{O}C showing the wide pore size distribution.

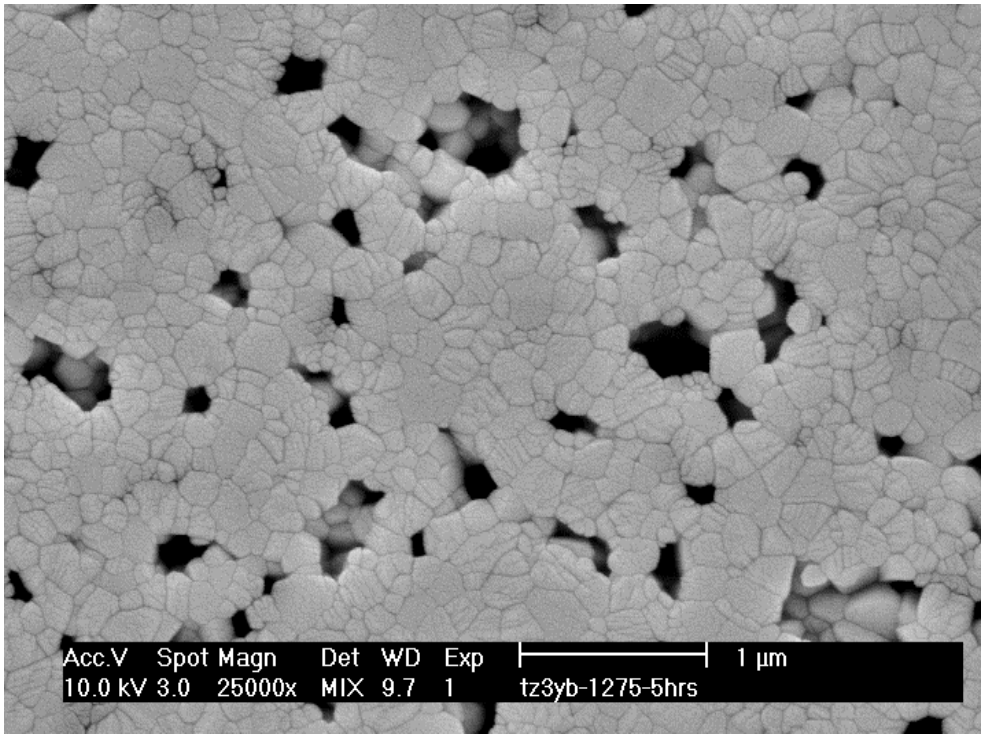

Figure 34 : The microstructure of a sample sintered for 5 hour at 1275^{O}C showing the dense areas between the widely spaced pores.

fine, aggregated powders are clear. To improve the situation, the spatial homogeneity of the green microstructure must be improved or the preferential elimination of fine pores must be avoided during sintering.

4.5 MICROSTRUCTURAL ANALYSES OF HPLT AND LPHT SAMPLES

Values of L_L (Solid Line Fraction) of HPLT and LPHT samples determined by image analysis were larger than Vv (Solid Volume Fraction value that calculated from the Archimedes method). The L_L values measured from SEM images and the Vv measured from Archimedes method are list in **Table 1**. If the images were representative, these measurements should give the same values. However, the solid line fractions are systematically higher suggesting that the images are not representative of the fraction of the porosity in the samples.

As for the LPLT, it is doubtful that the analysis is missing small pores. Instead, a sparse population of large-scale damages was found in SEM images of HPLT and LPHT samples as shown on **Figure 35** and **Figure 36**, which was not seen in the image of LPLT sample shown in **Figure 37**. **Figure 36** shows that the large irregular pores in the low density regions appear to break up and become less irregular as the sintering time is increased. This is thought to be responsible for the difference between the SVF measured by the Archimedes method and the L_L. This discrepancy suggests that images taken do not represent the average microstructure of the samples which complicates the interpretation. Observation of surface at low magnification suggests a composite structure of low-density heterogeneities trapped in a much higher solid volume fraction matrix. As sintering time increases, densification seems to be contributed mostly

by those low-density areas reducing the difference between L_L and Vs but not giving much change in L_L. (See **Figure 38**)

Table 1. Values of L_L and Vv

sample	Average L_L	Vv
HPLT 0.1 hours	0.959	0.797
HPLT 0.5 hours	0.975	0.844
HPLT 1 hour	0.985	0.866
HPLT 5 hours	0.981	0.921
LPHT 0.1 hours	0.928	0.791
LPHT 0.5 hours	0.955	0.847
LPHT 1 hour	0.950	0.867
LPHT 5 hours	0.973	0.926
LPHT 10 hours	0.990	0.950
LPLT 0.1 hours	0.761	0.707
LPLT 0.5 hours	0.821	0.761
LPLT 1 hour	0.841	0.79
LPLT 5 hours	0.922	0.855
LPLT 10 hours	0.930	0.887

Figure 39, **Figure 40**, **Figure 41**, **Figure 42** and **Figure 43** show the comparison of the average intercept lengths (grain length, pore length and pore separation) plotted against solid volume fraction measured from Archimedes method and against L_L from images analysis among LPLT, HPLT and HPLT. Figure 39 shows that the results of the average grain intercept appear to fall on a single relationship in which the grains grow slowly and suggests that there is little difference in

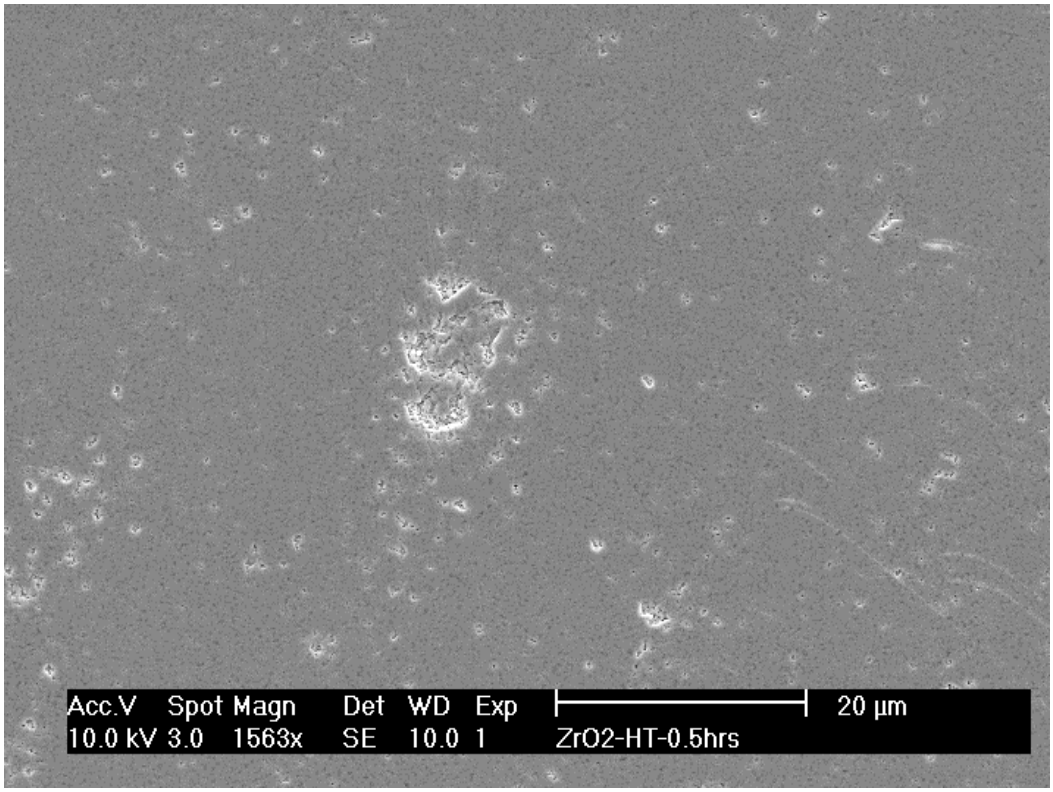

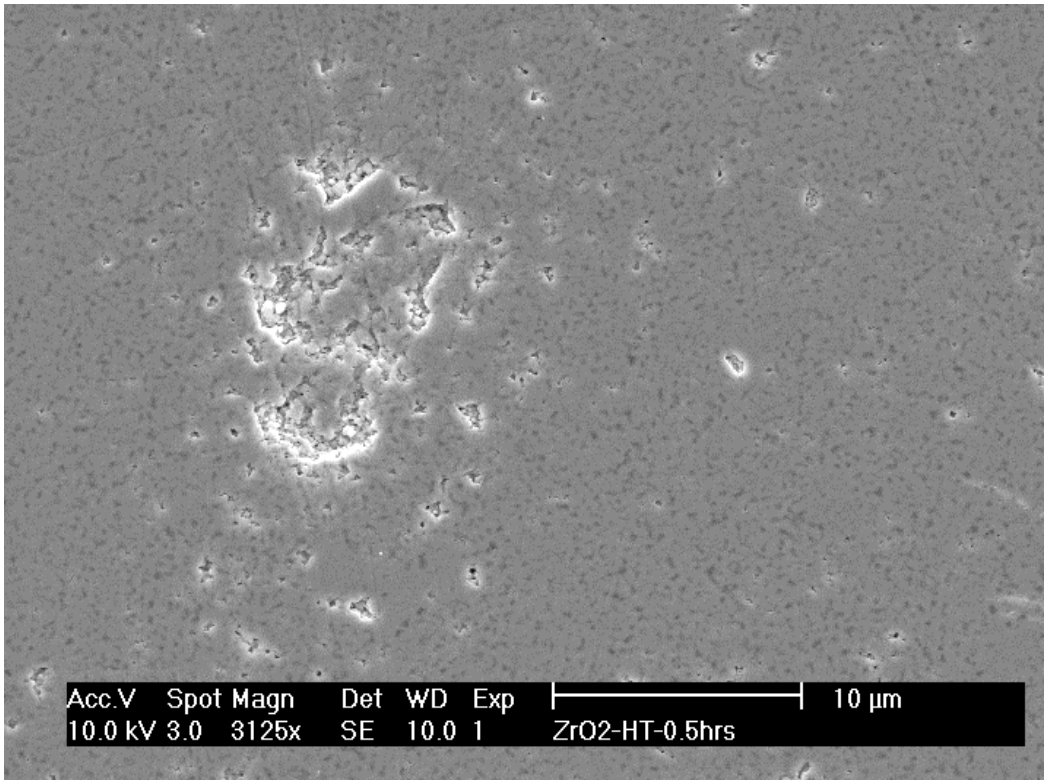

Figure 35 (a), (b): Damages were found in the low magnification SEM image of the polished cross section of HPLT sample sintered for 0.5 hours at 1315°C.

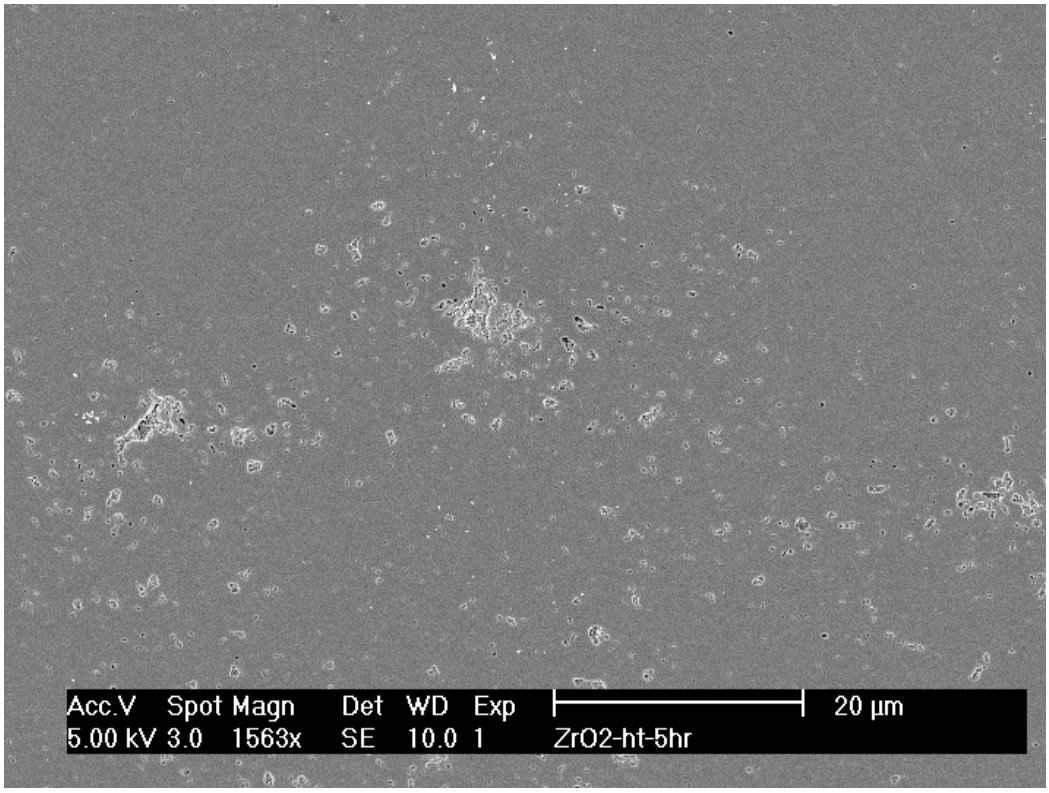

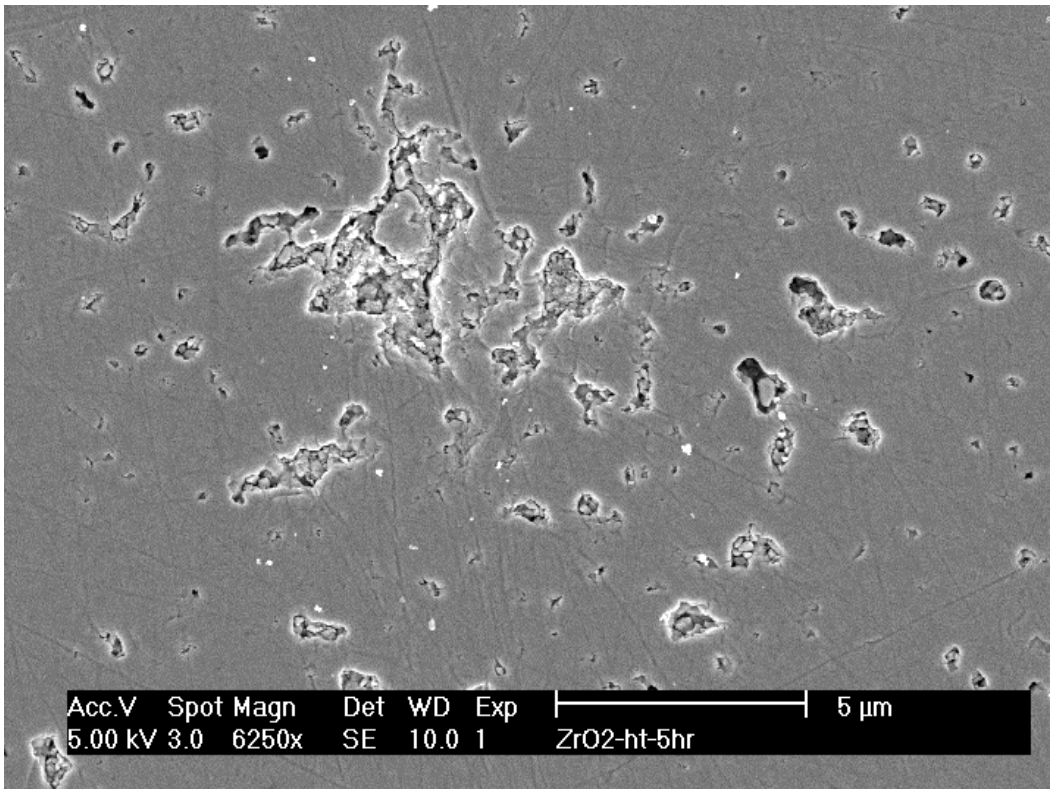

Figure 36 (a), (b): Damages were found in the low magnification SEM image of the polished cross section of HPLT sample sintered for 5 hours at 1275°C.

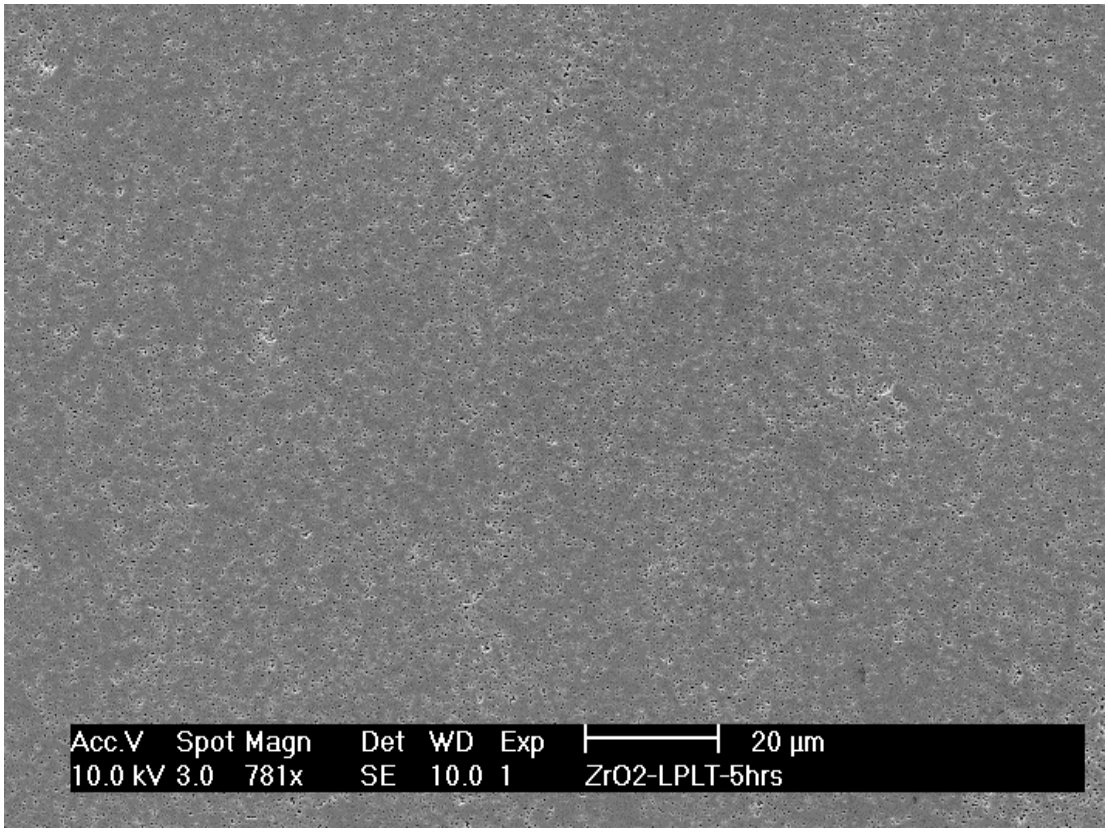

Figure 37 : Low magnification SEM image of LPLT sample showed there was no large damage on polished cross-section.

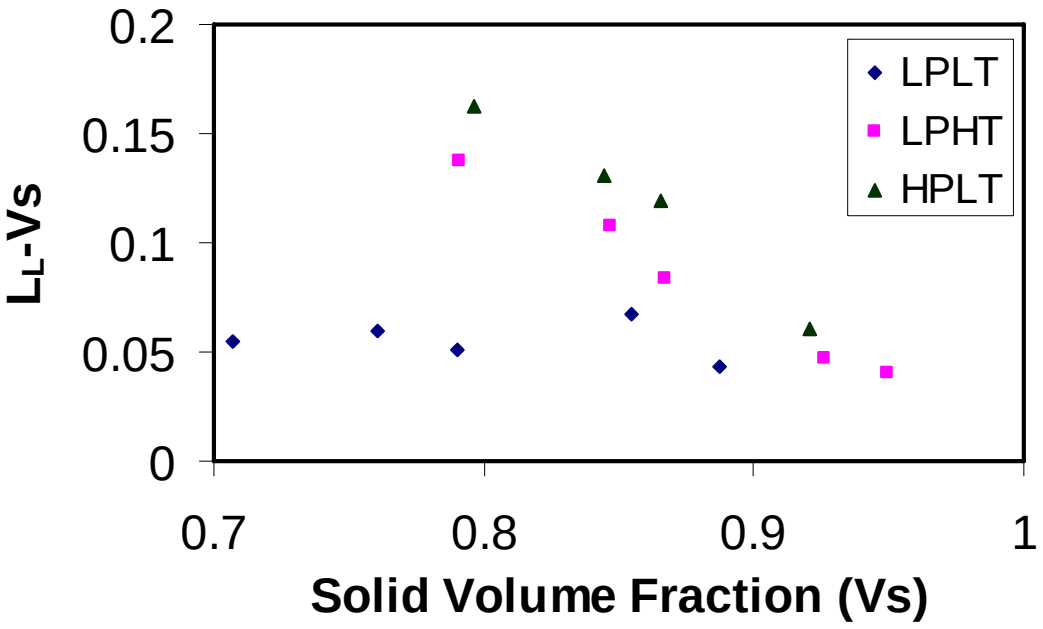

Figure 38 : The differences between global solid volume fraction and local solid line fraction are plotted against global solid volume fraction for LPLT, LPHT and HPLT samples.

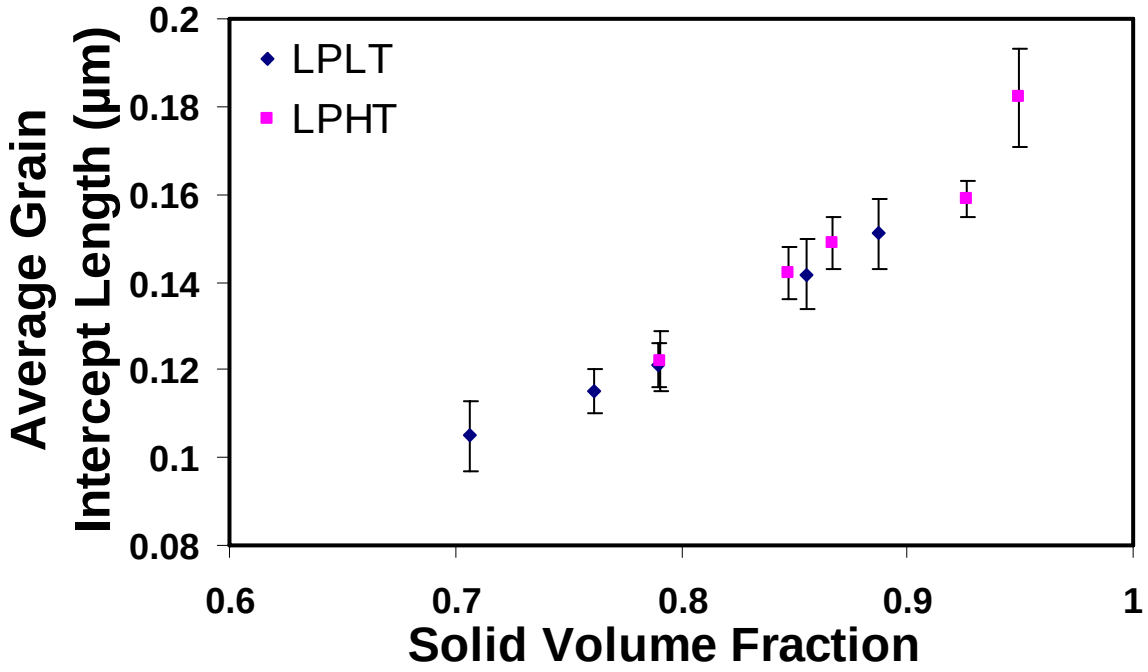

Figure 39 : The average intercept lengths plotted against solid volume fraction for the grains.

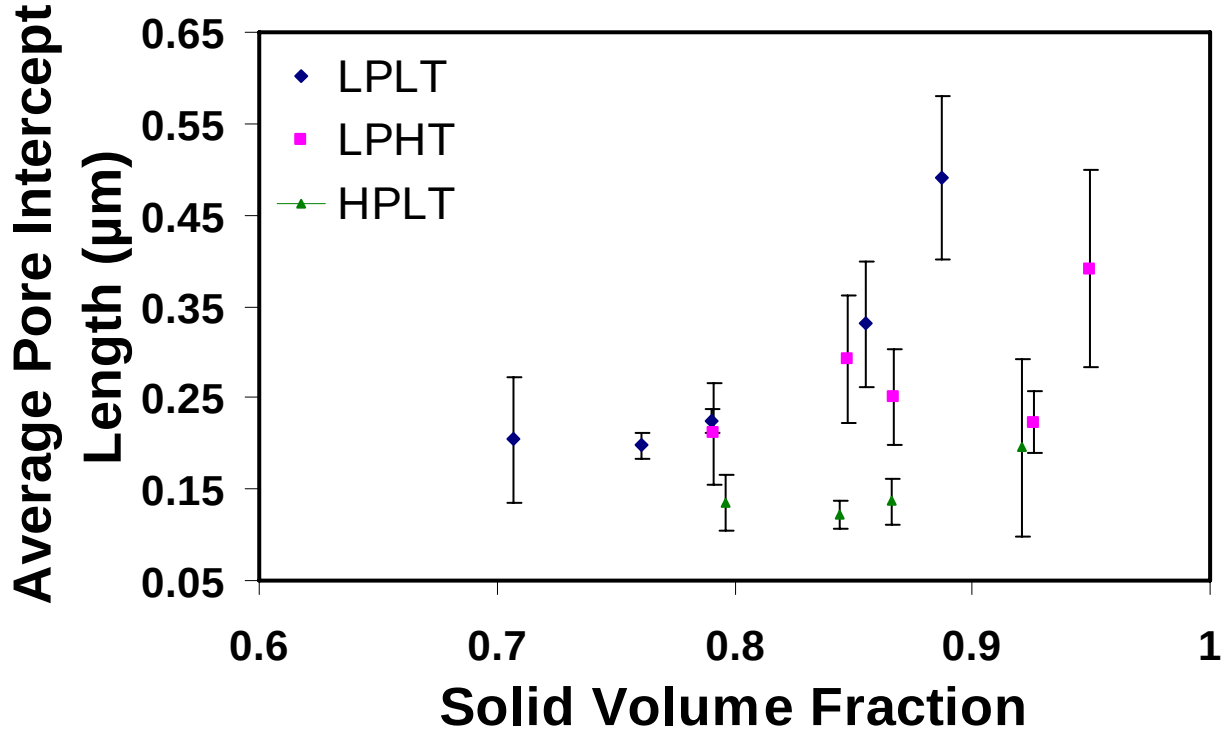

Figure 40 : The average pore intercept lengths plotted against solid volume fraction for the pores.

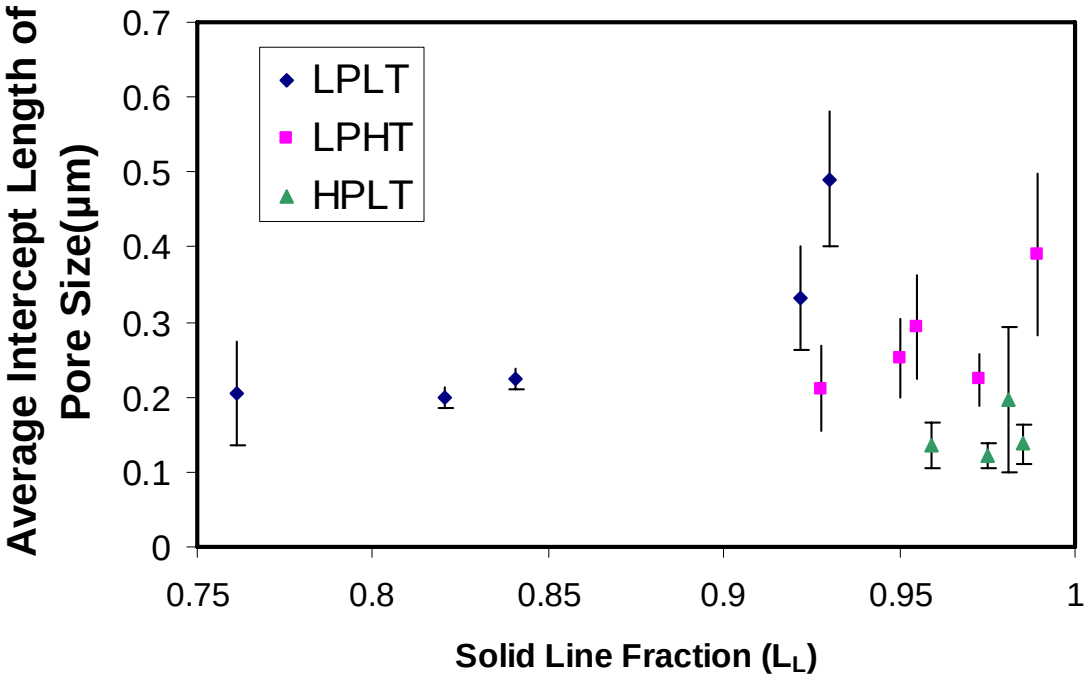

Figure 41 : The average pore intercept lengths plotted against solid line fraction for the pores.

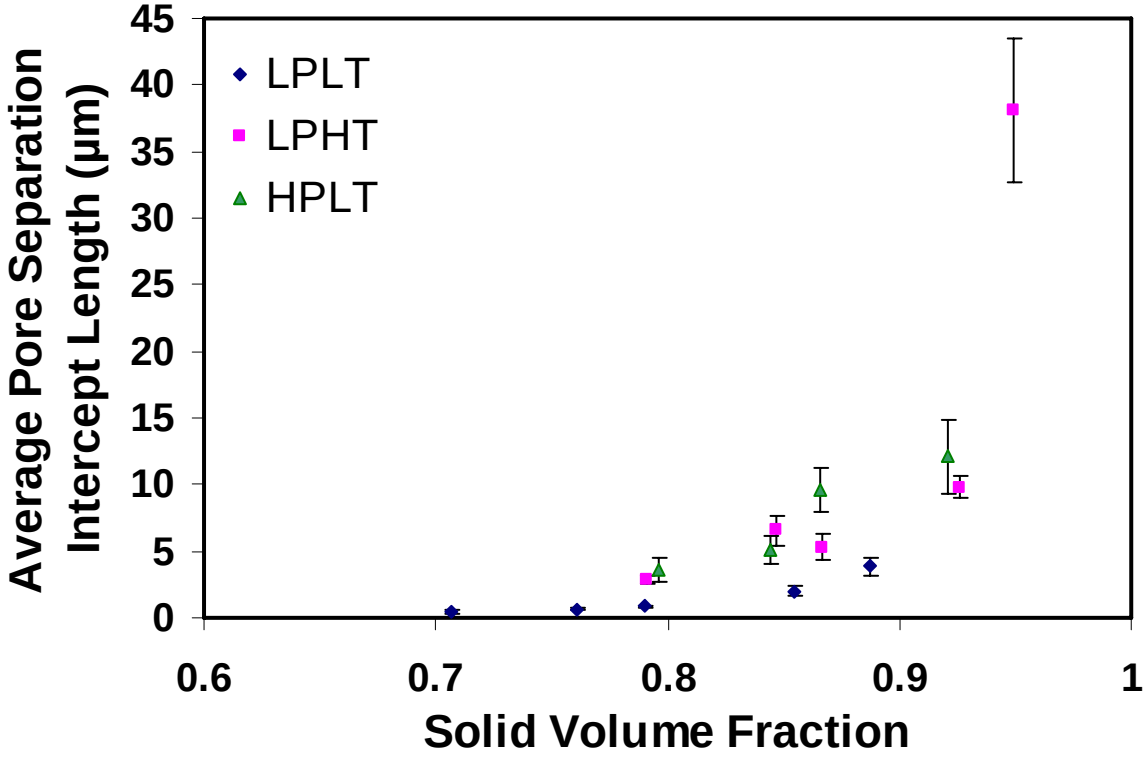

Figure 42 : The plot of average pore separation intercepts length against solid volume fraction.

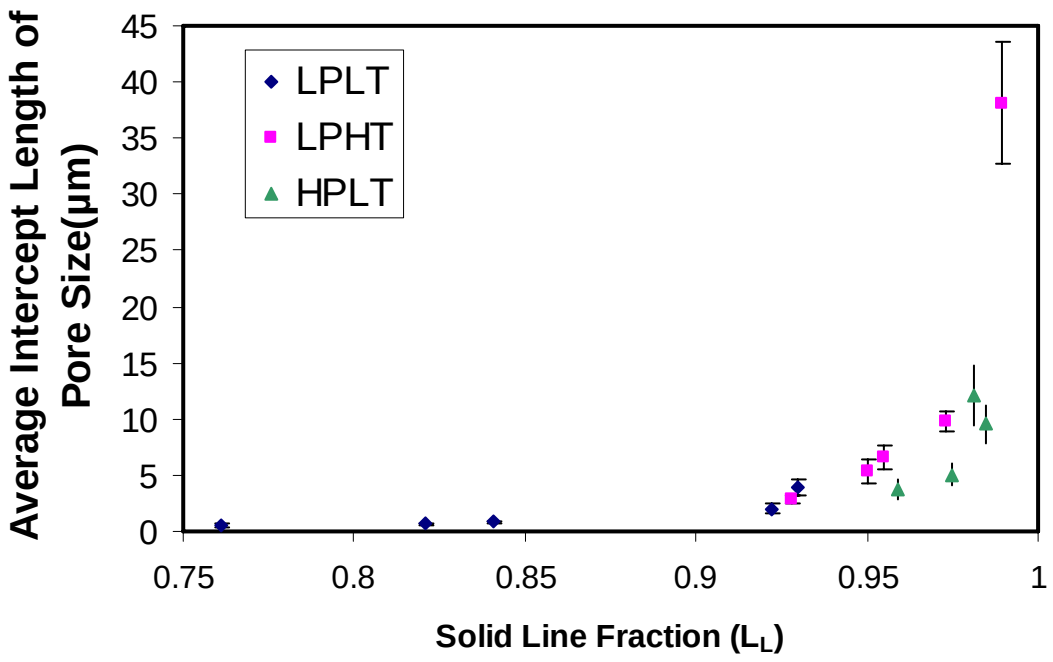

Figure 43 : The plot of average pore separation intercepts length against solid line fraction.

microstructure evolution as a function of density. In comparison to the average grain intercept, there is a great difference in the evolution of pore intercept and pore separation intercept depending on whether Vs or local density L_L is used. As shown in **Figure 42**, plots of λ_{PS} (mean pore separation intercept length) - solid volume fraction seems to not agree with master sintering curves which assumes microstructure v.s. density is constant for a given green microstructure and independent of thermal history. In contrast, **Figure 40** and **Figure 42** suggest LPHT coarsens at low density when compared to LPLT. This is contrary to what is expected since sintering at higher temperatures is expected to promote densification if coarsening is associated with a mass transport mechanism with a higher energy. However, when we plotted λ_{PS} and λ_P (mean pore size intercept length) against L_L (local density) as in **Figure 41** and **Figure 43**, a single curve is implied for groups LPLT and LPHT, which suggests that the pore separation v.s. local density is constant for a given green body process. It is not surprising that samples in group

HPLT do not fall onto the curve shared by LPLT and LPHT since the pressure used to produce green bodies was different, resulting in a different green microstructure with a higher green density.

A common microstructural evolution curve occurs when plotting λ_{PS} and λ_P against L_L, which suggests that the master sintering curve is followed at a "local scale" (scale of image). However, the densification behavior is a macroscopic measurement. It is therefore difficult to directly complete the two. Further work is required to develop microstructural measurements that represent the average behavior of the whole material. At that point the differences in microstructural evolution between LPLT on the one hand and LPHT and HPLT on the other, can be interpreted in terms of the densification behavior.

5.0 CONCLUSIONS

The evolution of the pore separation during the sintering of ZrO_2-3mol% Y_2O_3 showed evidence of coarsening that was not apparent from grain size measurements. The coarsening is thought to be due to low green density, which is assumed to be a manifestation of inhomogeneous particle packing. Sintering resulted in the formation of high density regions whose growth accompanied pore elimination through intermediate stage sintering. This coarsening process is a natural consequence of densification from low green density and does not require a coarsening of the grain structure resulting from a change in the mass transport mechanism. Higher pressing pressure (higher green density) or higher temperature in sintering resulted in more spatially heterogeneous microstructures by the growth of large regions with high solid volume fraction.

6.0 FUTURE WORKS

1. In the current thesis, the images could not well represent overall features of some samples, especially for HPLT and LPHT samples. Systematically random sampling needs to be done on lower magnification images in order to get more representative analysis and allow corrections with densification behavior in these materials.
2. Tessellation maps of LPLT samples have been done on this study. Additional tessellation maps of LPHT and HPLT samples would provide better understanding of the effect of green processing and thermal history on spatial heterogeneous in microstructural evolution. If low magnification images were unable to detect a significant population of fine pores, montage of several high magnification images may be necessary to give reprensentative results.
3. According to the master sintering curve theory, the evolution of the microstructural scale with the same green body processing is independent of thermal history. Examination of the microstructural evolution of two-step sintered nano-ceramics samples would be desirable since the implication of the second step is that densification and grain growth behavior are decoupled. This would be contrary to the assumptions of the master sintering curve.

BIBLIOGRAPHY

[1] Exner, H. E., "Principles of Single Phase Sintering," Reviews in Powder Metallurgy and Physical Ceramics, 1, 1-4, 1979, pp. 1-251.

[2] Burke, J. E. and J. H. Rosolowski, "Sintering," General Electric Technical Information Series, General Electric Company, Schenectady, NY, 1973.

[3] Olevsky, E. A., "Theory of Sintering; From Discrete to Continuum," Materials Science and Engineering, Vol. R23, No.2, 1998, pp. 41-100.

[4] Pask, J. A., and A. G. Evans ed., University Conference on Ceramics; Ceramic Microstructures '86: Role of Interface, "Powders, Interfaces, and Processing: Alumina as a Case Study by A. Roosen, S. Sumita and H. K. Bowen," Plenum, NY, 1987, pp. 433-446.

[5] Reed, J. S., Introduction to the Principles of Ceramic Processing, New York: Wiley-Interscience, 1988, p. 87.

[6] E. A. Olevsky "Theory of sintering, from discrete to continuum" *Mat. Sci. & Eng*., **R23**, 41-100 (1988).

[7] J. Besson and M. Abouaf (1992). "Rheology of porous alumina and simulation of hot isostatic pressing" *J. Am. Ceram. Soc.*, **75** [8], 2165-2172.

[8] R. K. Bordia and G. W. Scherer (1988). "On constrained sintering-I. constitutive model for a sintering body" *Acta Metall*., **36** [9], 2393-2397.

[9] W. D. Kingery and M. Berg (1955). "Study of the initial sintering of solids by viscous flow, evaporation-condensation and self diffusion" *J. Appl. Phys*., **26**, 1205.

[10] R. L. Coble (1961). "Sintering crystalline solids. I. intermediate and final state diffusion models" *J. Appl. Phys*., **32** [5], 787-792.

[11] H. Reidel and B. Blug (2001). A comprehensive model for the solid state sintering ad its application to silicon carbide. pp. 49-70, in *Multiscale Deformation and Fracture in*

Materials and Structures, the James R. Rice 60th Anniversary Volume. Edited by T. J. Chuang and J. W. Rudnicki. Klewer Academic Publishers, Boston.

[12] O. Gillia and D. Bouvard (2000). "Phenomenological analysis of densification kinetics during sintering: application to WC-Co mixtures" *Materials Science and Engineering*, **A279**, 185-191.

[13] P. Z. Cai, G. L. Green, (1997). "Determination of the mechanical response of sintering compacts by cyclic loading dilatometry" *J. Am. Ceram. Soc*., **80** [2], 445-452.

[14] V. Tikare, M. Braginsky, J. Arguello and T. Garino, (2003). "Numerical simulation of sintering at multiple length scales" Presented at 3rd *International conference on Science, Technology and Applications of Sintering*, September 15-17, State College, PA.

[15] Y. Chiang, D. Birnie III, W. D. Kingery, "Physical Ceramics: Principles for Ceramic Science and Engineering", p 394 John Wiley & Sons, Inc.

[16] C. Herring, "Surface Tension as a Motivation for Sintering", ch. 8, pp. 143-79 in *The Physics of Powder Metallurgy*. Edited by W. E. Kingston. McGraw-Hill, New York, 1951.

[17] Okamoto, J. Ieuji, Y. Yamada, K. Hayashi and T. Nishikawa, "Creep Deformation of Yttria-Stabilized Tetragonal Zirconia (Y-TZP)"; The *Amer. Ceram. Soc*., Columbus (OH) 1988, p. 565

[18] R. S. Gordon, "Ambipolar Diffusion and its application to Diffusion Creep"; pp. 445-64 in *Mass Transport Phenomena in Ceramics* (Materials Science Research, vol 9). Edited by A. R. Cooper and A. H. Heuer. Plenum, New York, 1975]

[19] Y. Sakka, Y. Oishi, and K. Ando, "Zr-Hf Interdiffusion in Polycrystalline Y_2O_3-(Zr+Hf)O_2"; *J. Mater. Sci.,* **17** [11] 3101-3105 (1982)

[20] M. Readey and D. Readey, "Sintering TiO2 in HCl atmosphere", *J. Am. Ceram. Soc.,* **70** [12] C-358-c361 (1987).

[21] R. J. McAfee, Jr., "A Study of Microstructural Evolution During Sintering Using Tessllation", Ph. D. Thesis, Univ. of Pittsburgh (2004).

[22] H. F. Fischmeister, and E. Arzt, "Densification of powders by particle deformation" Powder Metallurgy, **26** 82-88 (1983).

[23] M.F. Ashby, "A First Report on Sintering Diagrams," *Acta Metall.*, **22** 275-89 (1974).

[24] I. Nettleship, B. R. Patterson and W. S. Slaughter, "Evolution of Average Microstructureal Properties in the Final Stage Sintering of Alumina", *J. Am. Ceram. Soc.,* **86** [2] 252-56 (2003).

[25] W. S. Slaughter, I. Nettlship, M. D. Lehigh, and P. P. Tong, "A Quantitative Analysis of the Effects of Geometric Assumption in Sintering Models", *Acta Mater*., **45** [12] 5077-86 (1997).

[26] Weiser, M. W., and L. C. De Jonghe, "Rearrangement During Sintering in Two-Dimensional Arrays," *J. Am. Soc.*, Vol. 69, No. 11, 1986, pp. 822-826.

[27] R. W. Rice, W. R. Grace and Co. Conn., "Evaluation and Extension of Physical Property-Porosity Models Based on Minimum Solid Area" *J. of Mat. Sci.,* **31** (1996) 102-118.

[28] J. D. Hansen, R.P. Rusin, M.H. Teng and D.L. Johnson, "Combined Stage Sintering Model," *J. Am. Ceram. Soc.*, **75** 1129-35 (1992).

[29] R.T. DeHoff, "A Cell Model for Microstructural Evolution during Sintering", pp. 23-34 in *Sinfering and Heterogeneous Catalysis.* Edited by G.C. Kuczynski, A. E. Miller, and G. A. Sargent. Plenum Press, New York, 1984.

[30] H. Su and D.L. Johnson, "Master Sintering Curve: A practical Approach to Sintering," *J. Am. Ceram. Soc.*, **79** 3211-17 (1996).

[31] K. G. Ewsuk, D. T. Ellerby, G. B. DiAntonio, "Analysis of Nanocrystalline and Microcrystalline ZnO Sintering Using Master Sintering Curves", J. Am. Ceram. Soc., **89** 2003-2009 (2006).

[32] Ph. Buffat, J-P. Borel, *Phys. Rev.* A **13**, 2287 (1976)

[33] C. J. Coombes, Thesis, University of London, 1969. C. J. Coombes, *J. Phys. F* **2**, 441 (1972)

[34] J. Zheng and J. S Reed, "The Different Roles of Forming and Sintering on Densification of Powder Compacts," Am. Ceram. Soc. Bull., **71** [9] 1410–16 (1992).

[35] J. Zheng, J. S. Reed, "Effects of Particle Packing Characteristics on Solid-State Sintering" J. Am. Ceram. Soc., **72** 810-817 (1989).

[36] M.N. Rahaman, L.C. DeJonghe and M.Y. Chu, "Effect of Green Density on Densification and Creep During Sintering," *J. Am. Ceram. Soc*., **74** 514-19 (1991).

[37] C. P. Cameron, R. Raj, "Better Sintering through Green-State Deformation Processing ", J. Am. Ceram. Soc., 73 2032-37 (1990).

[38] J. Li and Y. Ye, "Densification and Grain Growth of Al2O3 Nanoceramics During Pressureless Sintering", J. Am. Cream. Soc., **89** [1] 139-143 (2006).

[39] X. Wang, P. Chen, and I. Chen, "Two-Step Sintering of Ceramics with Constant Grain-Size, I. Y_2O_3" J. Am. Cream. Soc., **89** [2] 431-437 (2006).

[40] E. E. Underwood, Quantitative Stereology, 1970, Addison-Wesley Publishing company.

[41] Weibel, E. R., Stereological Methods Volume 1, Practical Methods in Biological Morphometry New York: Academic Press, 1979.

[42] Vander Voort, G., ed., Applied Metallography, "Problem Solving Using Quantitative Stereology, by R. T. DeHoff" New York: Van Nustrand-Reinhold Company, 1986, pp. 89-99.

[43] Exner, H. E. and H. P. Hougardy, Quantitative Image Analysis of Microstructures: A Practical Guide to Techniques, Instrumentation, and Assessment of Materials, Stuttgart: Verlag, 1988, p. 10.

[44] Dehoff, R. T. and F. N. Rhines, "Quantitative Microscopy," McGraw-Hill, NY, 1968.

[45] Cahn, R. W. and P. Haasen ed., Physical Metallurgy: 4th Revised and Enhanced Edition, "Qualitative and Quantitative Surface Microscopy by H. E. Exner," Elsevier, 1996 pp. 996-1032.

[46] I. Nettleship, R. McAfee "Microstructural Pathway for the Densification of Slip Cast Alumina" Mater. Sci. Engi. A, **352** 287-293 (2003).

[47] J. Kanters, U. Eisele, H. Boder, J. Rodel " Continuum Mechanical Description of Sintering Nanocrystalline Zirconia" Advanced Engineering Materials, **3** 158-162 (2001).

[48] C.D. Sagel-Ransijn, A.J.A Winnubst, A.J. Burgraaf, H. Verweij, "Grain Growth in Ultra-fine Grained Y-TZP Ceramics," *J. Euro. Ceram. Soc.*, **17** 1133-1141 (1997).

[49] K.A. Berry and M.P. Harmer, "Effect of MgO Solute on Microstructure Development in Al_2O_3," *J. Am. Ceram. Soc*., **69** 143-149 (1986).

[50] R.J. McAfee and I. Nettleship, "A Mesoscale Description of Microstructure Evolution for the Sintering of Ceramics," *Acta Mater.,* **53** 4305-4311 (2005).

[51] B. M. Ennis, I. Nettleship and W. S. Slaughter, "A Three-Dimensional Model to Simulate Isotropic, Homogeneous Densification of Agglomerated Particle Arrangements," Submitted to *Acta Mater*.